

BRIGHT AND FAINT ENDS OF Ly α LUMINOSITY FUNCTIONS AT $z = 2$ DETERMINED BY THE SUBARU SURVEY: IMPLICATIONS FOR AGN, MAGNIFICATION BIAS, AND ISM H I EVOLUTION

AKIRA KONNO^{1,2}, MASAMI OUCHI^{1,3}, KIMHIKO NAKAJIMA⁴, FLORENT DUVAL¹,
HARUKA KUSAKABE², YOSHIKI ONO¹, AND KAZUHIRO SHIMASAKU^{2,5}

Submission : December 7, 2015

ABSTRACT

We present the Ly α luminosity functions (LFs) derived by our deep Subaru narrowband survey that identifies a total of 3,137 Ly α emitters (LAEs) at $z = 2.2$ in five independent blank fields. The sample of these LAEs is the largest, to date, and covers a very wide Ly α luminosity range of $\log L_{\text{Ly}\alpha} = 41.7 - 44.4 \text{ erg s}^{-1}$. We determine the Ly α LF at $z = 2.2$ with unprecedented accuracies, and obtain the best-fit Schechter parameters of $L_{\text{Ly}\alpha}^* = 5.29^{+1.67}_{-1.13} \times 10^{42} \text{ erg s}^{-1}$, $\phi_{\text{Ly}\alpha}^* = 6.32^{+3.08}_{-2.31} \times 10^{-4} \text{ Mpc}^{-3}$, and $\alpha = -1.75^{+0.10}_{-0.09}$ showing a steep faint-end slope. We identify a significant hump at the LF bright end ($\log L_{\text{Ly}\alpha} > 43.4 \text{ erg s}^{-1}$). Because all of the LAEs in the bright-end hump have (a) bright counterpart(s) either in the X-ray, UV, or radio data, this bright-end hump is not made by gravitational lensing magnification bias but AGNs. These AGNs allow us to derive the AGN UV LF at $z \sim 2$ down to the faint magnitude limit of $M_{\text{UV}} \simeq -22.5$, and to constrain the faint-end slope of AGN UV LF, $\alpha_{\text{AGN}} = -1.2 \pm 0.1$, that is flatter than those at $z > 4$. Based on the Ly α and UV LFs from our and previous studies, we find the increase of Ly α escape fraction $f_{\text{esc}}^{\text{Ly}\alpha}$ from $z \sim 0$ to 6 by two orders of magnitude. This large $f_{\text{esc}}^{\text{Ly}\alpha}$ increase can be explained neither by the evolution of stellar population nor outflow alone, but the evolution of neutral hydrogen H I density in inter-stellar medium that enhances dust attenuation for Ly α by resonance scattering. Our uniform expanding shell models suggest that the typical H I column density decreases from $N_{\text{H I}} \sim 7 \times 10^{19} (z \sim 0)$ to $\sim 1 \times 10^{18} \text{ cm}^{-2} (z \sim 6)$ to explain the large $f_{\text{esc}}^{\text{Ly}\alpha}$ increase.

Keywords: galaxies: evolution — galaxies: formation — galaxies: high-redshift —
galaxies: luminosity function, mass function

1. INTRODUCTION

Deep optical observations identify Ly α emitters (LAEs), most of which are continuum-faint star-forming galaxies with a prominent Ly α emission line (e.g., Cowie & Hu 1998; Hu et al. 1998; Rhoads et al. 2000; Steidel et al. 2000; Malhotra & Rhoads 2002; Hayashino et al. 2004; Matsuda et al. 2004; Taniguchi et al. 2005; Iye et al. 2006; Kashikawa et al. 2006; Shimasaku et al. 2006; Dawson et al. 2007; Gronwall et al. 2007; Murayama et al. 2007; Ouchi et al. 2008; Finkelstein et al. 2009; Guaita et al. 2010; Adams et al. 2011; Kashikawa et al. 2012; Shibuya et al. 2012; Yamada et al. 2012; Konno et al. 2014; Cassata et al. 2015; Sobral et al. 2015). LAEs are found at a wide redshift range of $z \sim 0 - 8$, and Ly α luminosity functions (LFs) of LAEs are used for probes of galaxy evolution and cosmic reionization (e.g., Ouchi et al. 2008, 2010; Kashikawa et al. 2011; Shibuya et al. 2012; Konno et al. 2014). In Ly α LFs, there is an important characteristics at the faint end. Galaxies at the faint end dominate in abundance, and faint-end slopes of Ly α LFs are determined by mass, star-formation activities, physical conditions of inter-stellar medium (ISM),

and feedback effects that are key for understanding galaxy evolution (e.g., Santos et al. 2004; Rauch et al. 2008). Although Ly α LFs at various redshifts have been derived by previous observations, faint-end slopes of the Ly α LFs are poorly constrained in contrast with those of UV LFs (e.g., Reddy & Steidel 2009; Oesch et al. 2010; Hathi et al. 2010; Sawicki 2012; Alavi et al. 2014; Bouwens et al. 2015; Parsa et al. 2015). The faint-end LF slopes are quantified with α , one of the three Schechter function parameters (Schechter 1976), depending on the rest of two parameters, characteristic Ly α luminosity $L_{\text{Ly}\alpha}^*$ and density $\phi_{\text{Ly}\alpha}^*$. Previous observational studies report α values for $z = 2 - 3$ Ly α LFs (e.g., Cassata et al. 2011), assuming a fixed parameter of $L_{\text{Ly}\alpha}^*$ or $\phi_{\text{Ly}\alpha}^*$. There are some studies that constrain α values with no assumptions (e.g., Gronwall et al. 2007; Hayes et al. 2010), but the uncertainties of the Schechter parameters are very large due to the small number of LAEs. Although α is a parameter depending on $L_{\text{Ly}\alpha}^*$ and $\phi_{\text{Ly}\alpha}^*$, so far, none of the observational studies have determined α simultaneously with $L_{\text{Ly}\alpha}^*$ and $\phi_{\text{Ly}\alpha}^*$ due to the small statistics of LAEs whose Ly α luminosity range is limited. In theoretical studies, Gronke et al. (2015) predict the three Schechter function parameters of Ly α LFs at $z = 3 - 6$, based on the measurements of UV LFs and Ly α EW probability distribution functions (PDFs), and argue that the faint-end slopes of the Ly α LFs are steeper than those of the UV LFs.

Another important characteristics of Ly α LFs is found at the bright end. The bright-end LFs are key for understanding massive-galaxy formation as well as faint active galactic nucleus (AGN; e.g., Gawiser et al. 2006; Ouchi et al. 2008; Zheng et al. 2013). Here, we define faint AGNs as

konno@icrr.u-tokyo.ac.jp

¹ Institute for Cosmic Ray Research, The University of Tokyo, Kashiwa-no-ha, Kashiwa 277-8582, Japan

² Department of Astronomy, Graduate School of Science, The University of Tokyo, Hongo, Bunkyo-ku, Tokyo, 113-0033, Japan

³ Kavli Institute for the Physics and Mathematics of the Universe (Kavli IPMU), WPI, The University of Tokyo, Kashiwa, Chiba 277-8583, Japan

⁴ Observatoire de Genève, Université de Genève, 51 Ch. des Maillettes, 1290 Versoix, Switzerland

⁵ Research Center for the Early Universe, Graduate School of Science, The University of Tokyo, Hongo, Bunkyo-ku, Tokyo, 113-0033, Japan

AGNs whose LFs overlap with non-AGN galaxy LFs in the luminosity ranges. The faint AGNs may play an important role in contributing to the UV radiation background (e.g., Giallongo et al. 2015). Faint AGNs are useful probes for quasar fueling lifetime, feedback, and duty cycle (e.g., Hopkins et al. 2006; Fiore et al. 2012). Faint AGNs are spectroscopically identified for most LAEs at $z \sim 3 - 4$ in the bright-end Ly α LF at $\log L_{\text{Ly}\alpha} \gtrsim 43.5 \text{ erg s}^{-1}$ (Gawiser et al. 2006; Ouchi et al. 2008). The bright-end LF includes an interesting physical effect, magnification bias. The magnification bias effect boosts luminosities of high- z galaxies by the gravitational lensing magnification given by foreground massive galaxies, and flattens the bright-end LFs (e.g. Mason et al. 2015; see Figure 3 of Wyithe et al. 2011). In the observational studies, humps of the bright-end Ly α LF are found at $z = 3 - 7$ (Gawiser et al. 2006; Ouchi et al. 2008; Matthee et al. 2015). In order to estimate the contributions of faint AGNs to the bright end LFs, it is important to investigate the properties of the bright-end galaxies with deep multiwavelength data such as X-ray, UV, and radio images.

The intermediate redshift range of $z \sim 2 - 3$ is the best for investigating faint- and bright-end Ly α LFs. This is because $z \sim 2 - 3$ is the lowest redshift range where Ly α emission fall in the optical observing window, which allows us to identify very faint LAEs as well as a large number of bright LAEs by fast optical surveys. By these reasons, in the past few years, various surveys have been conducted to study LAEs at $z \sim 2 - 3$. Although the Ly α LFs at $z \sim 3$ are well determined (e.g. Gronwall et al. 2007; Ouchi et al. 2008), those at $z \sim 2$ are derived with uncertainties larger than those at $z \sim 3$ due to difficulties of U -band observations at $\sim 3000 - 4000 \text{ \AA}$ to which Ly α emission lines of $z \sim 2$ objects are redshifted. Thus, the evolution of Ly α LFs from $z \sim 2$ to 3 is under debate. Nilsson et al. (2009) first claim that there is a possible evolution of LAE number densities between $z = 2.25$ and ~ 3 albeit with the large uncertainties originated from the small sample. Subsequent studies have identified $z \sim 2$ LAEs by narrowband imaging and spectroscopic observations, and discussed the evolution of Ly α LFs and the integrations of Ly α LFs, luminosity densities (LDs), at $z = 2 - 3$. Cassata et al. (2011) and Blanc et al. (2011) have carried out blank-field spectroscopy for LAEs at $2 < z < 6.6$ and $1.9 < z < 3.8$, respectively, and concluded no evolution of the Ly α LDs from $z = 2$ to 3. On the other hand, Ciardullo et al. (2012) show that the Ly α LF evolves from $z = 2.1$ to 3.1 significantly by the narrowband imaging surveys in ECDF-S (see also Guaita et al. 2010). Because the $z \sim 2$ LAE samples of these studies are limited in the LAE numbers (that are equal to or less than several hundreds) and the Ly α luminosity dynamic range (that is a factor of ~ 10), these discrepancies may be raised by the sample variances and the differences of Ly α luminosity coverages.

Evolution of Ly α LFs at $z \lesssim 2 - 3$ is also discussed extensively. Deharveng et al. (2008) claim that there is a substantial drop in the Ly α LFs from $z \sim 3$ to ~ 0.3 (see also Cowie et al. 2010, 2011; Barger et al. 2012; Wold et al. 2014). A similar evolutionary trend can be found in the Ly α escape fraction at $z \sim 0 - 6$ (e.g., Hayes et al. 2011, Blanc et al. 2011, Zheng et al. 2013). The physical origin of the rapid evolution may be dust attenuation within galaxies. From the observations of UV-continuum slope of Lyman break galaxies (LBGs), dust extinction, $E(B - V)$, decreases toward higher redshift (e.g., Bouwens et al. 2015). Because the Ly α escape fraction clearly depends on $E(B - V)$ (e.g., Kornei et al.

2010; Atek et al. 2014), dust extinction would explain the rapid evolution of the Ly α LF and Ly α escape fraction. To understand the major physical mechanisms related to the Ly α escape processes at high- z and its dependence on redshift, determining Ly α LFs at $z \sim 2$ is important.

In this paper, we present our analyses and results of the Ly α LFs at $z = 2.2$ based on our large LAE sample given by Subaru narrowband observations (Nakajima et al. 2012, 2013; see also Kusakabe et al. 2015). This sample contains 3,137 LAEs at $z = 2.2$ with a wide Ly α luminosity range of $41.7 \leq \log L_{\text{Ly}\alpha} \leq 44.4 \text{ erg s}^{-1}$, and enables us to examine the faint+bright ends and the evolution of Ly α LFs. We describe the details of our observations and our $z = 2.2$ LAE candidate selection in Section 2. We derive the Ly α LFs at $z = 2.2$, and compare the LFs with those of previous studies in Section 3. We investigate the Ly α LF and LD evolution from $z \sim 2$ to 3, and extend the discussion to the wider redshift range of $z \sim 0 - 8$ in Section 4. We finally discuss the physical origins of the bright-end of our $z = 2.2$ Ly α LFs, and the Ly α LD evolution at $z \sim 0 - 8$ in Section 5. Throughout this paper, we adopt AB magnitudes (Oke 1974) and concordance cosmology with a parameter set of $(h, \Omega_m, \Omega_\Lambda, \sigma_8) = (0.7, 0.3, 0.7, 0.8)$ consistent with the nine-year WMAP and Planck 2015 results (Hinshaw et al. 2013; Planck Collaboration et al. 2015).

2. OBSERVATIONS AND SAMPLE SELECTION

2.1. NB387 Observations

We have conducted a deep and large-area narrowband imaging survey for $z = 2.2$ LAEs with Subaru/Suprime-Cam (Miyazaki et al. 2002). For these observations, we have developed a new narrowband filter, NB387, with a central wavelength, λ_c , of 3870 \AA and an FWHM of 94 \AA to identify LAEs in the redshift range of $z = 2.14 - 2.22$. With our NB387 filter, we have observed five independent blank fields, the Subaru/XMM-Newton Deep Survey (SXDS) field (Furusawa et al. 2008), the Cosmic Evolution Survey (COSMOS) field (Scoville et al. 2007), the Chandra Deep Field South (CDFS; Giacconi et al. 2001), the Hubble Deep Field North (HDFN; Capak et al. 2004), and the SSA22 field (e.g., Steidel et al. 2000), in 2009 July 20 and December 14 - 16, 19 - 20. The SXDS field consists of five subfields of $\sim 0.2 \text{ deg}^2$, SXDS-C, -N, -S, -E, and -W (Furusawa et al. 2008). We cover these five SXDS subfields, COSMOS, CDFS, HDFN, and SSA22 by one pointing of Suprime-Cam whose field of view is $\sim 0.2 \text{ deg}^2$. We thus have NB387 imaging data in a total of nine pointing positions of Suprime-Cam. We summarize the details of our observations as well as image qualities in Table 1. In this study, we do not use the data of SXDS-E subfield due to the poor seeing size of $\simeq 2''$ in FWHM of point-spread function (PSF; see Table 1). During our observations, we have taken spectrophotometric standard stars Feige34, LDS749B, and G93-48 (Oke 1990) for photometric calibration. Each standard star has been observed more than twice under the photometric condition with air masses of 1.1 - 1.3.

2.2. Data Reduction

Our NB387 data are reduced with the Suprime-Cam Deep Field REDuction (SDFRED) package (Yagi et al. 2002; Ouchi et al. 2004). The data reduction process includes bias subtraction, flat fielding, distortion+atmospheric-dispersion correction, cosmic-ray rejection, sky subtraction, image shift-

Table 1
Summary of *NB387* Observations and Data

Band	Field	Exposure Time (hr)	PSF FWHM (arcsec)	Area ^a (arcmin ²)	m_{lim}^b (mag)	Date of Observations	Reference ^c
<i>NB387</i>	SXDS-C	3.2	0.88	587	25.7	2009 Dec 14–16	(1), (2)
	SXDS-N	2.5	0.70	409	25.6	2009 Dec 16	(1), (2)
	SXDS-S	2.5	0.85	775	25.7	2009 Dec 16	(1), (2)
	SXDS-E ^d	3.3	1.95	2009 Dec 19, 20	(1), (2)
	SXDS-W	1.8	1.23	232	25.1 ^e	2009 Dec 16, 19	(1), (2)
	COSMOS	4.5	0.97	845	26.1	2009 Dec 14–16	(2)
	CDFS	8.0	0.85	577	26.4	2009 Dec 14–15	(2), (3)
	HDFN	9.3	0.90	913	26.5	2009 Dec 14–16	(2)
	SSA22	1.0	0.91	800	24.9	2009 Jul 20	(2)
Total		36.1	...	5138
Archival Broadband Data							
$u^*(U)$	SXDS-C		0.85		26.9		(4)
	SXDS-N		0.85		26.9		(4)
	SXDS-S		0.85		26.9		(4)
	SXDS-E		0.85		26.9		(4)
	SXDS-W		0.85		26.9		(4)
	COSMOS		0.90		27.2		(5)
	CDFS		0.80		28.0		(6)
	HDFN		1.29		26.4 ^e		(7)
	SSA22		1.00		26.3		(8)
<i>B</i>	SXDS-C		0.80		27.5		(9)
	SXDS-N		0.84		27.8		(9)
	SXDS-S		0.82		27.8		(9)
	SXDS-E		0.82		27.5		(9)
	SXDS-W		0.78		27.7		(9)
	COSMOS		0.95		27.5		(10)
	CDFS		0.97		26.9		(11)
	HDFN		0.77		26.3 ^e		(7)
	SSA22		1.02		26.7		(8)

^a The effective area for the $z = 2.2$ LAE selection. The effective areas of SXDS-C, -N, -S, -E, and -W are limited by the u^* image which covers 77% of SXDS (see Nakajima et al. 2012 for details). The area of CDFS is constrained by the deep U -band image taken with VLT/VIMOS (Nonino et al. 2009).

^b The 5σ limiting magnitude in a circular aperture with a diameter of $2''.0$.

^c (1) Nakajima et al. (2012); (2) Nakajima et al. (2013); (3) Kusakabe et al. (2015); (4) S. Foucaud et al., in preparation (see also Nakajima et al. 2012); (5) McCracken et al. (2010); (6) Nonino et al. (2009); (7) Capak et al. (2004); (8) Hayashino et al. (2004); (9) Furusawa et al. (2008); (10) Capak et al. (2007); (11) Hildebrandt et al. (2006).

^d We do not use the *NB387* image of SXDS-E since the PSF FWHM is relatively large.

^e We use $2''.5$ and $3''.0$ diameter apertures for *NB387* of SXDS-W and U B of HDFN, respectively, due to bad seeings.

ing, and stacking. In cosmic-ray rejection process, we use *LA.COSMIC* (van Dokkum 2001). Before the image shifting, we mask out bad pixels and satellite trails.

After the stacking process, we calculate photometric zero points of the *NB387* images from the standard-star data (see Section 2.1). We estimate the errors in the photometric zero points based on colors of stellar objects in the two-color diagram of *NB387* and two adjacent broadbands in the blue and red sides of *NB387* (e.g., $u^* - \text{NB387}$ and $B - \text{NB387}$ in SXDS). We compare the colors of stellar objects and the template 175 Galactic stars (Gunn & Stryker 1983), and regard the offsets as the uncertainties. The inferred uncertainties are $\lesssim 0.05$ mag, which are negligibly small for our study.

All of the *NB387* images, except the SXDS-E data, have the PSF FWHM of $0''.7 - 1''.2$, and reach the 5σ limiting magnitudes of $24.9 - 26.5$ in a $2''.0$ -diameter circular aperture. We summarize the qualities of these reduced *NB387* images in Table 1. We mask out the imaging regions that are contaminated with halos of bright stars, CCD blooming, and the low signal-to-noise ratio pixels near the edge of the images. After the masking, the total survey area is $5,138 \text{ arcmin}^2$, i.e. $\simeq 1.43 \text{ deg}^2$. If we assume a simple top-hat selection function for LAEs whose redshift distribution is defined by the FWHM of *NB387*, this total survey area corresponds to the comoving

volume of $\simeq 1.32 \times 10^6 \text{ Mpc}^3$.

In our analysis and LAE selection, we use archival u^* - (or U -) and B -band data as well as our *NB387* images. In the SXDS field, the u^* - and B -band data are taken with CFHT/MegaCam (S. Foucaud et al., in preparation) and Subaru/Suprime-Cam (Furusawa et al. 2008), respectively. The u^* - and B -band images in the COSMOS field are obtained with CFHT/MegaCam (McCracken et al. 2010) and Subaru/Suprime-Cam (Capak et al. 2007), respectively. We use VLT/VIMOS U -band (Nonino et al. 2009) and MPG 2.2m Telescope/WFI B -band (Hildebrandt et al. 2006) images in CDFS (see Kusakabe et al. 2015 for more details), and KPNO 4m Telescope/MOSAIC prime focus camera U -band and Subaru/Suprime-Cam B -band images in HDFN (Capak et al. 2004). In SSA22 field, we use the u^* -band data of CFHT/MegaCam and B -band data of Subaru/Suprime-Cam (Hayashino et al. 2004). The properties of these optical broadband data are also summarized in Table 1. Note that in CDFS, Nakajima et al. (2013) do not use the VLT/VIMOS U -band image, but only the MPG 2.2m Telescope/WFI U -band image (Gawiser et al. 2006; Cardamone et al. 2010) that is significantly shallower than the VLT/VIMOS U -band data. The deep VLT/VIMOS U -band image allows us to remove foreground contamination efficiently, although the area cov-

erage of VLT/VIMOS U -band data is smaller than that of MPG 2.2m Telescope/WFI U -band data. We thus use the deep VLT/VIMOS U -band image.

To measure colors of objects precisely, we align our $NB387$ images with the broadband data using bright stellar objects commonly detected in the $NB387$ and the broadband images. After the image alignment process, we match the PSF sizes of broadband and narrowband images in each field, referring to these stellar objects.

2.3. Photometric Sample of $z = 2.2$ LAEs

Our source detection and photometry are performed with SExtractor (Bertin & Arnouts 1996). We identify sources that are made of contiguous > 5 pixels whose counts are above the $> 2\sigma$ brightness of the background fluctuations in our $NB387$ images. We obtain a circular aperture magnitude of SExtractor's MAG_APER with an aperture's diameter of $2''.5$ in the SXDS-W field, $3''.0$ in the HDFN field, and $2''.0$ in the other fields, and define a 5σ -detection limit magnitude with the aperture size in each field. The different aperture diameters are applied, because the PSF sizes of the homogenized images in the SXDS-W and HDFN are large, $1''.23$ and $1''.29$, respectively. We use the aperture magnitudes to calculate colors of the sources, and adopt MAG_AUTO of SExtractor for our total magnitudes. All magnitudes of the sources are corrected for Galactic extinction of $E(B - V) = 0.020, 0.018, 0.008, 0.012$, and 0.08 in the SXDS, COSMOS, CDFS, HDFN, and SSA22 fields, respectively (Schlegel et al. 1998). We thus obtain source catalogs that contain 42,995 (SXDS), 31,401 (COSMOS), 24,451 (CDFS), 36,236 (HDFN), and 8,942 (SSA22) objects with the aperture magnitudes brighter than the 5σ -detection limit magnitudes.

We select $z = 2.2$ LAE candidates based on narrowband excess colors of $u^* - NB387$ (or $U - NB387$) and $B - NB387$, in the same manner as Nakajima et al. (2012) who present the first results of the $NB387$ observations in the SXDS field. Figure 1 presents two color diagrams of $B - NB387$ versus $u^* - NB387$ (or $U - NB387$). In this figure, we plot colors of model galaxies and Galactic stars to define the selection criteria for $z = 2.2$ LAE candidates. Based on Figure 1, we apply the color criteria (Nakajima et al. 2012, 2013; Kusakabe et al. 2015)

$$u^* - NB387 > 0.5 \text{ and } B - NB387 > 0.2 \\ \text{in SXDS, COSMOS, and SSA22,} \quad (1)$$

$$U - NB387 > 0.5 \text{ and } B - NB387 > 0.2 \\ \text{in CDFS,} \quad (2)$$

$$U - NB387 > 0.5 \text{ and } B - NB387 > 0.2 \\ \text{in HDFN} \quad (3)$$

to obtain $z = 2.2$ LAE candidates whose rest-frame $\text{Ly}\alpha$ equivalent width, EW_0 , are $\text{EW}_0 \gtrsim 20 - 30 \text{ \AA}$. After the visual inspection to remove spurious sources, such as ghosts, bad pixels, surviving cosmic rays (see Nakajima et al. 2012 for more details), we identify 3,137 LAE candidates in our survey fields. The sample of these LAE candidates is referred to as the full sample. This is so far the largest LAE sample in the large area field surveys (cf. 187 and 250 LAEs at $z \simeq 2.2$ with $\text{EW}_0 > 20 \text{ \AA}$ observed by Nilsson et al. 2009 and Guaita et al. 2010, respectively). We summarize the details of the full sample in Table 2.

We make a subsample with the uniform criterion of $\text{Ly}\alpha$ $\text{EW}_0 > 60 \text{ \AA}$ to compare the $\text{Ly}\alpha$ LF at $z = 3.1$ of Ouchi et al.

(2008) (see Section 4.1), and refer to the subsample as the $\text{EW} > 60$ sample. We apply the color criteria of

$$u^* - NB387 > 0.9 \text{ and } B - NB387 > 0.2 \\ \text{in SXDS, COSMOS, and SSA22,} \quad (4)$$

$$U - NB387 > 0.8 \text{ and } B - NB387 > 0.2 \\ \text{in CDFS,} \quad (5)$$

$$U - NB387 > 1.0 \text{ and } B - NB387 > 0.2 \\ \text{in HDFN} \quad (6)$$

for the $\text{EW} > 60$ sample. After the visual inspection, we obtain 985 LAE candidates for the $\text{EW} > 60$ sample that is summarized in Table 2.

3. LUMINOSITY FUNCTION

3.1. Contamination

We investigate the contamination sources of our LAE samples that are low- z emitters whose emission lines are redshifted to the bandpass of $NB387$. The major strong emission that enters into the $NB387$ bandpass is $[\text{OII}]\lambda 3727$. However, our survey area of $5,138 \text{ arcmin}^2$ (Section 2.2) corresponds to the comoving volume of $1.22 \times 10^3 \text{ Mpc}^3$ for $[\text{OII}]$ emitters at $z = 0.04$, which is three orders of magnitude smaller than the survey volume of our $z = 2.2$ LAEs ($1.32 \times 10^6 \text{ Mpc}^3$). Moreover, the color criterion defined by Equations (1)-(3) corresponds to a relatively large rest-frame EW limit of $\gtrsim 70 \text{ \AA}$ for $z = 0.04$ $[\text{OII}]$ emitters. Ciardullo et al. (2013) examine $[\text{OII}]$ LFs and EW distributions at $z \sim 0.1$ and find that the $[\text{OII}]$ EW distribution has an exponential scale of 8.0 \AA , which is significantly smaller than our selection criterion for $[\text{OII}]$ emitters (i.e., $\text{EW}_0 \sim 70 \text{ \AA}$). Based on our survey parameters (see Sections 2.2-2.3) and the Ciardullo et al.'s $[\text{OII}]$ LF and EW distribution, the expected number of $[\text{OII}]$ emitters at $z = 0.04$ in our full sample is $\sim 3 \times 10^{-2}$. Therefore, the probability of the $[\text{OII}]$ emitter contamination would be very small.

Nevertheless, spectroscopic follow-up observations for our LAEs have been conducted with Magellan/IMACS, MagE, and Keck/LRIS by Nakajima et al. (2012), Hashimoto et al. (2013), Shibuya et al. (2014) and M. Rauch et al., in preparation. A total of 43 LAEs are spectroscopically confirmed. These spectroscopic observations find no foreground interlopers such as $[\text{OII}]$ emitters at $z = 0.04$ that show $[\text{OIII}]\lambda 5007$ emission at 5200 \AA (see e.g. Nakajima et al. 2012). Although these spectroscopic redshift confirmations are limited to bright LAEs with $NB387 \lesssim 24.5$, we estimate the contamination rate is less than a few percent. Thus, the effects of contamination sources are negligibly small in our LAE samples.

3.2. Detection Completeness

We evaluate detection completeness in each field by Monte-Carlo simulations, following the procedures of Konno et al. (2014). We randomly distribute a total of $\sim 5,000$ artificial sources mimicking LAEs in each $NB387$ image, and detect the artificial sources in the same manner as the real source identifications (Section 2.3). Here, we assume that LAEs at $z = 2.2$ are point sources, and use profiles obtained by the stack of 500 bright point sources in each $NB387$ image. We define the detection completeness as a fraction of the numbers of the detected artificial sources to all of the input artificial sources. We obtain the detection completeness as a function of $NB387$ magnitude, repeating this process with various

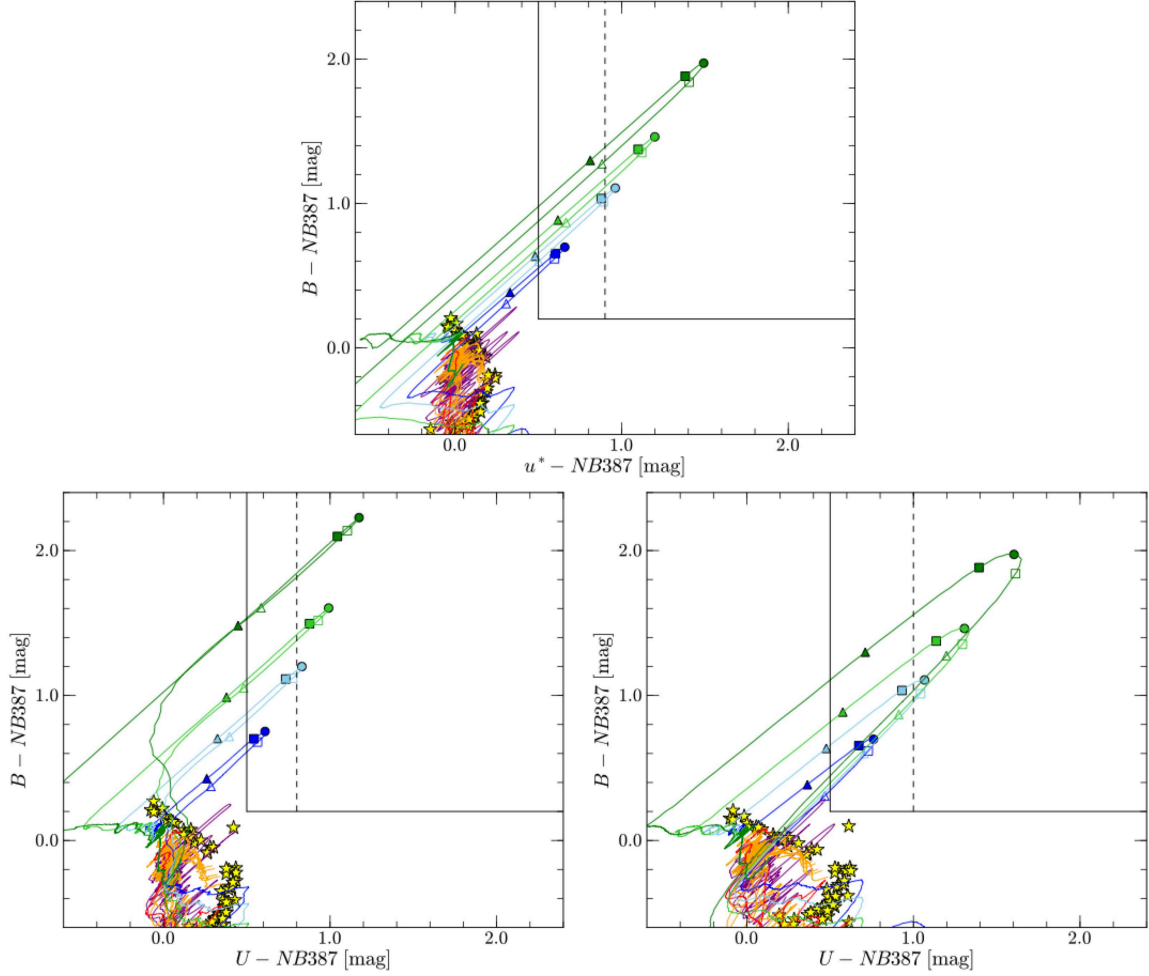


Figure 1. Two color diagrams for the selection of $z = 2.2$ LAEs: $B - NB387$ vs. $u^* - NB387$ for SXDS, COSMOS, and SSA22 (top); $B - NB387$ vs. $U - NB387$ in CDFS (bottom left); $B - NB387$ vs. $U - NB387$ in HDFN (bottom right). The solid lines in blue, light blue, light green, and green represent the color tracks of redshifted model LAE SEDs with $\text{Ly}\alpha$ $\text{EW}_0 = 30, 60, 100$, and 200\AA , respectively. These models are produced by using the Bruzual & Charlot (2003) population synthesis model where we adopt a 30 Myr simple stellar population with Salpeter IMF and adding a $\text{Ly}\alpha$ emission. We apply the Madau (1995) prescription to take into account the inter-galactic medium (IGM) absorption. The symbols on these tracks correspond to $z = 2.14$ (filled triangles), 2.16 (filled squares), 2.18 (filled circles), 2.20 (open squares), and 2.22 (open triangles). The red and orange curves show the tracks of three elliptical (age of 2, 5, 13 Gyr) and six spiral (S0, Sa, Sb, Sc, Sd, and Sdm) galaxies from the SWIRE template library (Polletta et al. 2007), respectively. The purple solid lines indicate six templates of nearby starburst galaxies (Kinney et al. 1996). These elliptical, spiral and starburst template galaxies are redshifted from $z = 0.0$ up to 2.0 with a step of $\Delta z = 0.001$. The yellow star marks are 175 Galactic stars given by Gunn & Stryker (1983). The black solid and dashed lines represent the color criteria to select our $z = 2.2$ LAE candidates whose $\text{Ly}\alpha$ EWs are larger than $20 - 30\text{\AA}$ and 60\AA , respectively.

magnitudes of the input artificial sources. Figure 2 shows the results of these Monte-Carlo simulations. We find that the detection completeness is typically $\gtrsim 90\%$ for relatively bright sources ($NB387 < 24.5$) in all fields, and $\sim 50\%$ at around the 5σ limiting magnitude of $NB387$ in each field (see Table 1).

3.3. Cosmic Variance

To include field-to-field variation in the error bar of our $\text{Ly}\alpha$ LFs, we calculate the cosmic variance uncertainty, σ_g , with

$$\sigma_g = b_g \sigma_{\text{DM}}(z, R), \quad (7)$$

where b_g and $\sigma_{\text{DM}}(z, R)$ are the bias parameter of galaxies and the density fluctuation of dark matter in a sphere with a radius R at a redshift z , respectively. We estimate $\sigma_{\text{DM}}(z, R)$ with the growth factor, following Carroll et al. (1992) with the transfer function given by Bardeen et al. (1986) (see also Mo & White 2002). The value of $\sigma_{\text{DM}}(z, R)$ at $z = 2.2$ is estimated to be 0.055. Since Guaita et al. (2010) find the bias

parameter of $b_g = 1.8 \pm 0.3$ from the clustering analysis of $z = 2.1$ LAEs in the ECFD-S field, we adopt this value for b_g in Equation (7). We thus obtain the cosmic variance uncertainty of $\sigma_g \simeq 0.099$.

3.4. Ly α Luminosity Functions

We derive the $\text{Ly}\alpha$ LFs at $z = 2.2$ from the full and $\text{EW} > 60$ samples, adopting the classical method of the $\text{Ly}\alpha$ LF derivation (Ouchi et al. 2010; Konno et al. 2014) whose accuracy is confirmed by Monte-Carlo simulations (Shimasaku et al. 2006; Ouchi et al. 2008).

We calculate $\text{Ly}\alpha$ EWs of our LAEs from the aperture magnitudes of $NB387$ and B , and obtain $\text{Ly}\alpha$ luminosities of our LAEs from these EWs and the total magnitudes of $NB387$. We estimate photometric errors of $\text{Ly}\alpha$ luminosities, performing Monte-Carlo simulations under the assumption that the SEDs of LAEs have a $\text{Ly}\alpha$ line located at λ_c of $NB387$ and a flat UV continuum (i.e., $f_\nu = \text{const.}$) with the inter-galactic medium (IGM) absorption of Madau (1995). We calculate volume

Table 2
Photometric Sample of $z = 2.2$ LAEs

Field	All LAE sample ^a	X-ray detection ^b	UV detection ^c	Radio detection ^d	Culled sample ^e
The full sample					
SXDS-C	277	3 [3]	3 [3]	0 [0]	274
SXDS-N	239	4 [4]	5 [4]	0 [0]	234
SXDS-S	374	5 [3]	5 [4]	1 [1]	367
SXDS-W	44	0 [0]	0 [0]	0 [0]	44
COSMOS	642	20 [10]	10 [10]	7 [5]	619
CDFS	423	6 [4]	...	6 [4]	415
HDFN	967	7 [1]	11 [1]	...	950
SSA22	171	...	3 [...]	...	168
Total ^f	3137 (1576)	45	37	14	3071 (1538)
The EW > 60 sample					
SXDS-C	103	2 [2]	2 [2]	0 [0]	101
SXDS-N	69	0 [0]	0 [0]	0 [0]	69
SXDS-S	129	1 [0]	1 [0]	0 [0]	127
SXDS-W	6	0 [0]	0 [0]	0 [0]	6
COSMOS	194	9 [4]	4 [4]	3 [3]	184
CDFS	142	3 [2]	...	2 [2]	139
HDFN	298	2 [0]	0 [0]	...	296
SSA22	44	...	1 [...]	...	43
Total	985	17	8	5	965

^a The numbers of $z = 2.2$ LAE candidates after the color selection and rejection of spurious objects.

^b The numbers of $z = 2.2$ LAE candidates detected in the X-ray data. The values in square brackets represent the numbers of objects that are also detected in the UV and/or radio data.

^c The numbers of $z = 2.2$ LAE candidates detected in the UV data taken by *GALEX*. The values in square brackets show the numbers of objects that are also detected in the X-ray and/or radio data.

^d The numbers of $z = 2.2$ LAE candidates detected in the radio data. The values in square brackets show the numbers of objects that are also detected in the X-ray and/or UV data.

^e The numbers of $z = 2.2$ LAE candidates with no counterpart detection(s) in multiwavelength data of X-ray, UV, and radio.

^f The total numbers of $z = 2.2$ LAE candidates. The values in parentheses indicate the total numbers of LAEs found in the SXDS and COSMOS fields.

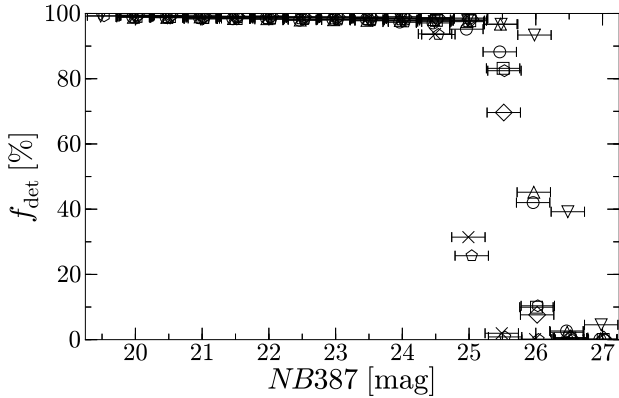


Figure 2. Detection completeness, f_{det} , of our *NB387* images. The symbols represent the completeness in a magnitude bin of $\Delta m = 0.5$ mag for the SXDS-C (squares), SXDS-N (diamonds), SXDS-S (hexagons), SXDS-W (pentagons), COSMOS (circles), CDFS (inverted triangles), HDFN (triangles), and SSA22 (cross marks) fields. For presentation purposes, we slightly shift all the points along the abscissa.

number densities of LAEs in a $\text{Ly}\alpha$ luminosity bin, dividing the number counts of LAEs by our comoving survey volume ($\simeq 1.32 \times 10^6 \text{ Mpc}^3$; see Section 2.2) under the assumption of the top-hat filter transmission curve. We correct these number densities for the detection completeness estimated in Section 3.2.

The top panel of Figure 3 presents the best estimate of our $\text{Ly}\alpha$ LF at $z = 2.2$ from the full sample. We also plot the $\text{Ly}\alpha$ LF measurements derived from each-field data. The error bars

of the $\text{Ly}\alpha$ LF include uncertainties from Poisson statistics and cosmic variance obtained in Section 3.3. For the Poisson errors, we use the values in columns “0.8413” in Table 1 and 2 of Gehrels (1986) for the upper and lower limits of the Poisson errors, respectively. The best estimate $\text{Ly}\alpha$ LF covers a $\text{Ly}\alpha$ luminosity range of $\log L_{\text{Ly}\alpha} = 41.7 - 44.4 \text{ erg s}^{-1}$. Our $\text{Ly}\alpha$ luminosity limit of $\log L_{\text{Ly}\alpha} = 41.7 \text{ erg s}^{-1}$ ($5.0 \times 10^{41} \text{ erg s}^{-1}$) is one order of magnitude fainter than the $L_{\text{Ly}\alpha}^*$ values at $z = 3 - 6$ ($\log L_{\text{Ly}\alpha, z=3-6}^* \sim 42.8 \text{ erg s}^{-1}$; Shimasaku et al. 2006; Gronwall et al. 2007; Ouchi et al. 2008).

We fit a Schechter function (Schechter 1976) to our $z = 2.2$ $\text{Ly}\alpha$ LF by minimum χ^2 fitting. The Schechter function is defined by

$$\phi_{\text{Ly}\alpha}(L_{\text{Ly}\alpha})dL_{\text{Ly}\alpha} = \phi_{\text{Ly}\alpha}^* \left(\frac{L_{\text{Ly}\alpha}}{L_{\text{Ly}\alpha}^*} \right)^\alpha \exp \left(-\frac{L_{\text{Ly}\alpha}}{L_{\text{Ly}\alpha}^*} \right) d \left(\frac{L_{\text{Ly}\alpha}}{L_{\text{Ly}\alpha}^*} \right), \quad (8)$$

(see Section 1 for the definitions of the parameters). We include $\text{Ly}\alpha$ LF measurements of Blanc et al. (2011) and Cassata et al. (2011) for our fitting. We determine three parameters of the Schechter function simultaneously, and obtain the best-fit Schechter parameters of $\alpha = -1.75_{-0.09}^{+0.10}$, $L_{\text{Ly}\alpha}^* = 5.29_{-1.13}^{+1.67} \times 10^{42} \text{ erg s}^{-1}$ and $\phi_{\text{Ly}\alpha}^* = 6.32_{-2.31}^{+3.08} \times 10^{-4} \text{ Mpc}^{-3}$. This is the first time to determine three Schechter function parameters with no fixed parameter(s), and the faint-end slope of α is reasonably well constrained. Table 3 presents these best-fit Schechter parameters. We show the

best-fit Schechter function in the top panel of Figure 3, and error contours of the Schechter parameters in Figure 4.

The top panel of Figure 3 shows an excess of the number densities beyond the best-fit Schechter function at the bright-end of $\log L_{\text{Ly}\alpha} \gtrsim 43.4$ erg s $^{-1}$. We refer to this excess as bright-end hump. Ouchi et al. (2008) find that there is a possible excess of the Ly α LFs at $z = 3.1$ and 3.7 similar to the bright-end hump, and claim that 100% of LAEs host AGNs at the bright ends of $\log L_{\text{Ly}\alpha} > 43.6$ and 43.4 erg s $^{-1}$, respectively, based on the large-area LAE survey with the multiwavelength data set. Thus, the bright-end hump of our $z = 2.2$ Ly α LF may be produced by AGNs. To examine whether our LAEs at the bright end include AGNs, we use the multiwavelength data of X-ray, UV, and radio available in the SXDS, COSMOS, CDFS, HDFN, and SSA22 fields. For the X-ray data, we use the *XMM-Newton* source catalog in the SXDS field (Ueda et al. 2008), the *Chandra* 1.8 Ms catalog in the COSMOS field (Elvis et al. 2009), the *Chandra* 4 Ms source catalog in the CDFS field (Xue et al. 2011), and the *Chandra* 2 Ms catalog in the HDFN field (Alexander et al. 2003). The typical sensitivity limits of these X-ray data are $\sim 10^{-16}$ - 10^{-15} erg cm $^{-2}$ s $^{-1}$ for the SXDS and COSMOS fields, and $\sim 10^{-17}$ - 10^{-16} erg cm $^{-2}$ s $^{-1}$ for the CDFS and HDFN fields. We use *GALEX* FUV and NUV images for the UV data, and obtain these images from the Multimission Archive at STScI (see also Zamojski et al. 2007 for the COSMOS field). The *GALEX* images reach the 3σ detection limit of ~ 25 - 26 mag. The Very Large Array 1.4 GHz source catalogs of Simpson et al. (2006) (SXDS), Schinnerer et al. (2007) (COSMOS), and Miller et al. (2013) (CDFS) are used for the radio data. These radio data reach an rms noise level of ~ 10 μ Jy beam $^{-1}$. We find that a majority of our bright LAEs are detected in the multiwavelength data, and summarize the numbers of these LAEs in Table 2. Under the column of “culled sample” in Table 2, we show the numbers of LAEs with no counterpart detection(s) in the X-ray, UV, and radio data. As shown in Table 2, the SXDS and COSMOS fields have the data that cover all of the X-ray, UV, and radio wavelengths. Moreover, the X-ray, UV, and radio data spatially cover the entire fields of SXDS and COSMOS with the similar sensitivities. We make a subsample that is composed of all 1,576 LAEs found in the SXDS and COSMOS fields, and refer to this subsample as SXDS+COSMOS/All. We then make another subsample consisting of 1,538 LAEs with no multiwavelength counterpart detection(s) in the SXDS and COSMOS fields, which is dubbed SXDS+COSMOS/Culled.

In the bottom panel of Figure 3, we plot the Ly α LFs derived from the subsamples of SXDS+COSMOS/All and SXDS+COSMOS/Culled. We fit the Schechter function to these Ly α LFs and the complementary Ly α LF data of Blanc et al. (2011) and Cassata et al. (2011), and presents the best-fit Schechter parameter sets and the error contours in Table 3 and Figure 4, respectively. Comparing the Ly α LF of the SXDS+COSMOS/All subsample with that of the full sample, in Figures 3 and 4, we find that the Ly α LF of the SXDS+COSMOS/All subsample is consistent with that of the full sample within the uncertainties. Figure 4 indicates that the Schechter fitting results of the full sample and the SXDS+COSMOS/All subsample are very similar with the one of the SXDS+COSMOS/Culled subsample, which are determined in the wide luminosity range of $\log L_{\text{Ly}\alpha} = 41.7 - 44.4$ erg s $^{-1}$. However, there are no objects in SXDS+COSMOS/Culled subsample that has $\log L_{\text{Ly}\alpha} >$

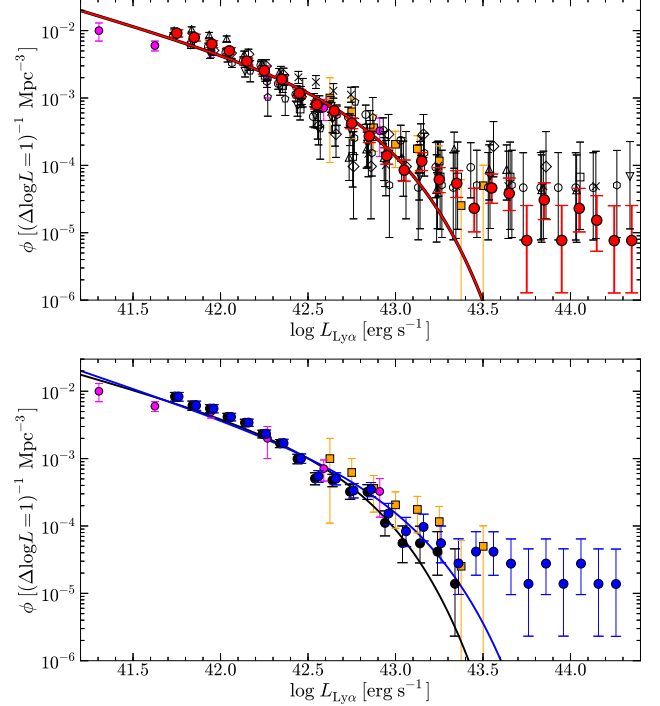


Figure 3. *Top:* Ly α LF of our $z = 2.2$ LAEs with a luminosity bin of $\Delta \log L_{\text{Ly}\alpha} = 0.1$. The red filled circles represent the Ly α LF derived from the full sample and the red solid curve denotes the best-fit Schechter function. The black open symbols show the Ly α LFs in the SXDS-C (squares), SXDS-N (diamonds), SXDS-S (hexagons), SXDS-W (pentagons), COSMOS (circles), CDFS (inverted triangles), HDFN (triangles), and SSA22 (cross marks) fields. For clarity, we slightly shift all the points along the abscissa. The magenta filled circles and orange filled squares are the results from Cassata et al. (2011) and Blanc et al. (2011), respectively. *Bottom:* Ly α LF at $z = 2.2$ derived from the SXDS and COSMOS fields. The blue and black filled circles represent the Ly α LFs from the SXDS+COSMOS/All and SXDS+COSMOS/Culled subsamples, respectively. The blue and black solid curves show the best-fit Schechter functions of our best-estimate Ly α LFs using the SXDS+COSMOS/All and SXDS+COSMOS/Culled subsamples, respectively. The magenta filled circles and orange filled squares are the same as the top panel of this figure.

43.4 erg s $^{-1}$. The Ly α LF of SXDS+COSMOS/Culled subsample does not have a bright-end hump such found in those of the full sample and the SXDS+COSMOS/All subsample. These comparisons suggest that the bright-end hump of the $z = 2.2$ Ly α LF is originated from AGNs that are bright in the X-ray, UV, and/or radio wavelength(s). We discuss more details of the bright-end hump in Sections 5.1 and 5.2.

3.5. Comparison with Previous Studies

We compare our best-estimate Ly α LF with those from previous studies at $z \sim 2$. In Figure 5, we plot the Ly α LFs obtained by narrowband imaging surveys (Hayes et al. 2010; Ciardullo et al. 2012; see also Guaita et al. 2010) and blank-field spectroscopic surveys (Blanc et al. 2011; Cassata et al. 2011; Ciardullo et al. 2014). Hayes et al. (2010) carry out deep imaging with two narrowband filters covering Ly α and H α lines, and report the Ly α LF as well as the Ly α escape fraction of $z = 2.2$ LAEs. Ciardullo et al. (2012) derive the Ly α LF of $z = 2.1$ LAEs based on the narrowband data of Guaita et al. (2010). In both studies, the Ly α EW criterion of narrowband excess colors is $\text{EW}_0 = 20\text{\AA}$, comparable to our studies. Blanc et al. (2011) and Ciardullo et al. (2014) obtain the Ly α LFs by the spectroscopic observations of the Hobby Eberly Telescope Dark Energy Experiment (HETDEX) Pilot

Table 3
Schechter Parameters for Full and Culled Samples

Sample	α	$L_{\text{Ly}\alpha}^*$ ($10^{42} \text{ erg s}^{-1}$)	$\phi_{\text{Ly}\alpha}^*$ (10^{-4} Mpc^{-3})
Full ^a	$-1.75^{+0.10}_{-0.09}$	$5.29^{+1.67}_{-1.13}$	$6.32^{+3.08}_{-2.31}$
SXDS+COSMOS/All ^b	$-1.87^{+0.10}_{-0.08}$	$7.83^{+3.22}_{-2.34}$	$2.99^{+2.26}_{-1.27}$
SXDS+COSMOS/Culled ^c	$-1.72^{+0.12}_{-0.11}$	$4.28^{+1.47}_{-0.99}$	$7.33^{+3.89}_{-2.83}$

^a The full sample, which is constructed from the SXDS, COSMOS, CDFS, HDFN, and SSA22 fields.

^b The sample of LAEs found in the SXDS and COSMOS fields.

^c The sample of LAEs with no multiwavelength counterpart detection(s) in the SXDS and COSMOS fields.

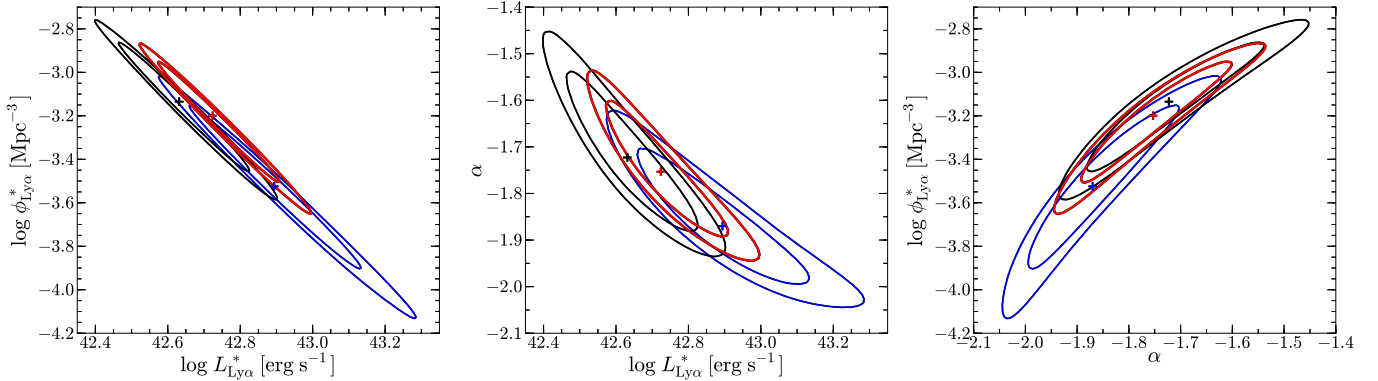


Figure 4. Error contours of Schechter parameters, $L_{\text{Ly}\alpha}^*$, $\phi_{\text{Ly}\alpha}^*$ and α . The red contours represent our best-estimate Ly α LF based on the full sample. The blue and black contours show our best-estimate Ly α LFs using the SXDS+COSMOS/All and SXDS+COSMOS/Culled subsamples, respectively. The inner and outer contours denote the 68% and 90% confidence levels, respectively. The red, blue and black crosses are the best-fit Schechter parameters for our best-estimate Ly α LFs based on the full sample, SXDS+COSMOS/All subsample, and SXDS+COSMOS/Culled subsample, respectively.

Survey for LAEs at $1.9 < z < 3.8$ and $1.90 < z < 2.35$, respectively. Cassata et al. (2011) make a spectroscopic sample of LAEs at $2 < z < 6.6$ with the VIMOS VLT Deep Survey. In these spectroscopic surveys, most of LAEs have a Ly α EW greater than 20\AA . Table 4 summarizes the best-fit Schechter parameters (and Ly α luminosity ranges of the observations) given by our and the previous studies.

In Figure 5 and Table 4, we find that our $z = 2.2$ Ly α LF is generally consistent with those of the previous studies in the measurement ranges of the Ly α luminosity overlaps. However, there exist some noticeable differences. The Ly α LF of Ciardullo et al. (2012) is not similar to ours and Blanc et al. (2011) at the bright end, but similar to ours and Cassata et al. (2011) at the faint end. In contrast, the Ly α LF of Ciardullo et al. (2014) is not consistent with ours and Cassata et al. (2011) at the faint end, but consistent with ours and Blanc et al. (2011) at the bright end. Because Ciardullo et al. (2012) and Ciardullo et al. (2014) cover the reasonably wide Ly α luminosity ranges of $42.1 < \log L_{\text{Ly}\alpha} < 42.7 \text{ erg s}^{-1}$ and $41.9 < \log L_{\text{Ly}\alpha} < 43.7 \text{ erg s}^{-1}$, respectively, the origins of these differences at the bright and faint ends are not clear.

As clarified in Table 4, most of the previous studies fit the Schechter function to their Ly α LFs, assuming a fixed parameter. Hayes et al. (2010) constrain three Schechter parameters simultaneously, but the uncertainties of these parameters are large due to small statistics (see also Gronwall et al. 2007 for $z \sim 3$). Our study constrains three Schechter parameters simultaneously, using the large LAE sample of 3,137 LAEs covering the wide Ly α luminosity range ($\log L_{\text{Ly}\alpha} =$

$41.7 - 44.4 \text{ erg s}^{-1}$).

4. Ly α LUMINOSITY FUNCTION AND DENSITY EVOLUTION

4.1. Evolution of Ly α LFs

In this section, we first examine the evolution of Ly α LFs at $z \sim 2 - 3$ and then investigate the evolution from $z \sim 0$ to 6 with the compilation of the Ly α LF data taken from the literature.

For the $z \sim 3$ data, we use the Ly α LF of Ouchi et al. (2008). The $z = 3.1$ Ly α LF of Ouchi et al. (2008) is derived in the same manner as ours (see Sections 3.2–3.4). Because the EW criterion of Ouchi et al. (2008) is $\text{EW} \gtrsim 60\text{\AA}$, we compare the Ly α LF obtained from our $\text{EW} > 60$ sample (Section 2.3). The Ly α LF and the best-fit Schechter function (parameters) for the $\text{EW} > 60$ sample are presented in the left panel of Figure 6 (Table 5). The left panel of Figure 6 indicates that the Ly α LFs increase from $z \sim 2$ to 3.

To quantify this evolutionary trend, we show the error contours of the Schechter parameters of our $z = 2.2$ Ly α LF (red contours) and the $z = 3.1$ Ly α LF (blue contours) in the right panel of Figure 6. Here, we apply our best-fit $z = 2.2$ Ly α LF slope of $\alpha = -1.8$ (Section 3.4) to the $z = 3.1$ LF result, because α is not determined in the $z = 3.1$ Ly α LF. Comparing the $z = 2.2$ and 3.1 error contours in the right panel of Figure 6, we find that the Ly α LF increases from $z = 2.2$ to 3.1 at the $> 90\%$ confidence level. However, this increase is not large, only within a factor of ~ 2 (see Table 5). Note that there exist no systematic errors raised by the analysis technique in the comparison of our $z = 2.2$ and Ouchi et al.’s

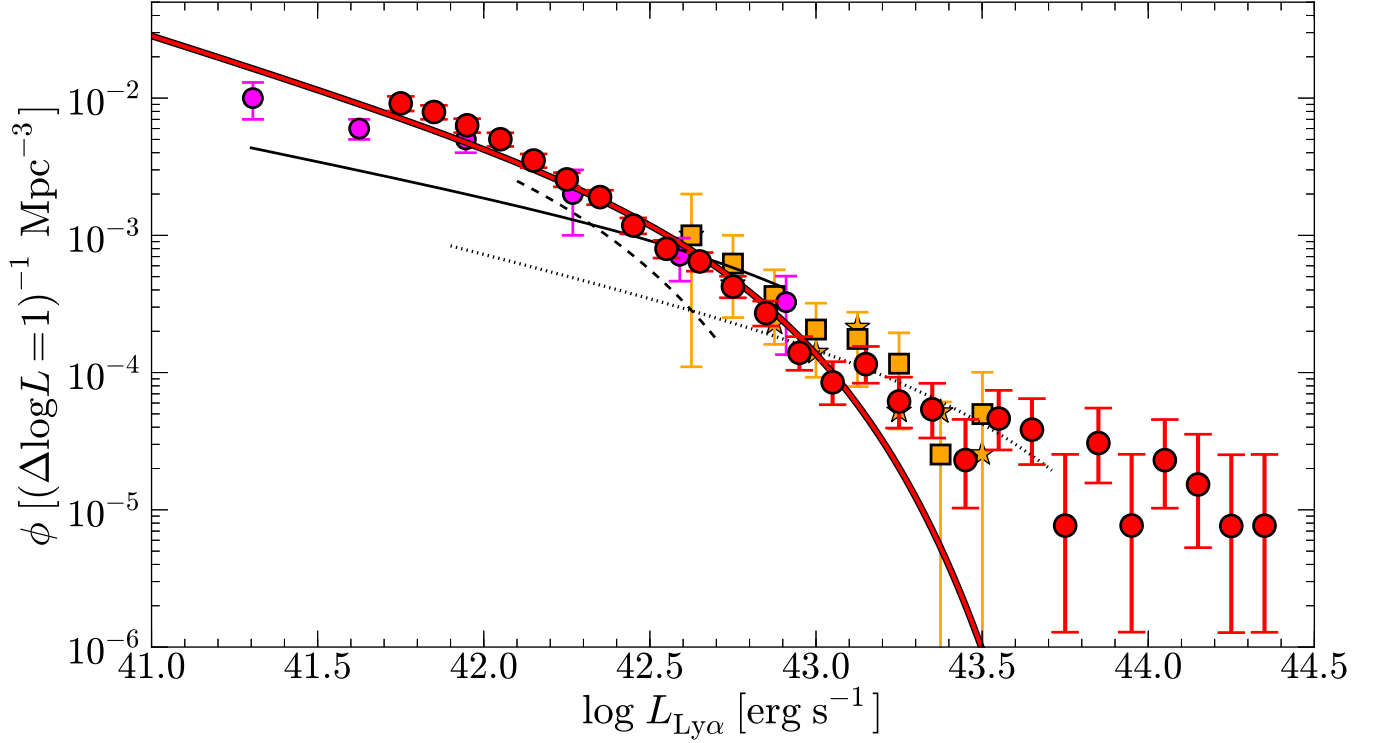


Figure 5. Comparison of our $z = 2.2$ Ly α LF with the previous measurements of Ly α LF at $z \sim 2$. The red filled circles denote our Ly α LF and the red solid curve is the best-fit Schechter function, which are the same as the top panel of Figure 3. The magenta filled circles represent the Ly α LF given by Cassata et al. (2011) at $2 < z < 3.2$. The orange stars and squares show the LFs by Blanc et al. (2011) based on the spectroscopic surveys of LAEs at $1.9 < z < 2.8$ and $1.9 < z < 3.8$, respectively. The black solid, dashed, and dotted lines are the best-fit Schechter functions obtained by Hayes et al. (2010), Ciardullo et al. (2012), and Ciardullo et al. (2014), respectively. Since the previous Ly α LF estimates are limited in the ranges of $\log L_{\text{Ly}\alpha} = 41.3 - 42.9$ erg s $^{-1}$ (Hayes et al. 2010), $42.1 - 42.7$ erg s $^{-1}$ (Ciardullo et al. 2012), and $41.9 - 43.7$ erg s $^{-1}$ (Ciardullo et al. 2014), we show the black lines within these ranges.

Table 4
Schechter Parameters of Previous $z \sim 2$ LAE Studies

Study	α	$L_{\text{Ly}\alpha}^*$ (10^{42} erg s $^{-1}$)	$\phi_{\text{Ly}\alpha}^*$ (10^{-4} Mpc $^{-3}$)	$\log L_{\text{Ly}\alpha}$ range
This work	$-1.75^{+0.10}_{-0.09}$	$5.29^{+1.67}_{-1.13}$	$6.32^{+3.08}_{-2.31}$	41.7 – 44.4
Hayes et al. (2010)	-1.49 ± 0.27	$14.5^{+15.7}_{-7.54}$	$2.34^{+5.42}_{-1.64}$	41.3 – 42.9
Blanc et al. (2011)	-1.7 (fixed)	$16.3^{+94.6}_{-10.8}$	$1.0^{+5.4}_{-0.9}$	42.6 – 43.6
Cassata et al. (2011)	-1.6 ± 0.12	5.0 (fixed)	$7.1^{+2.4}_{-1.8}$	41.2 – 43.1
Ciardullo et al. (2012)	-1.65 (fixed)	$2.14^{+0.68}_{-0.52}$	$13.8^{+1.7}_{-1.5}$	42.1 – 42.7
Ciardullo et al. (2014)	-1.6 (fixed)	$39.8^{+98.2}_{-16.4}$	0.36 ^a	41.9 – 43.7

^a Ciardullo et al. (2014) do not show the errors of $\phi_{\text{Ly}\alpha}^*$, although they present the uncertainties of the total number densities of LAEs integrated down to $\log L_{\text{Ly}\alpha} = 41.5$ erg s $^{-1}$, $\phi_{\text{tot}} = 9.77^{+3.11}_{-2.36} \times 10^{-4}$ Mpc $^{-3}$.

$z = 3.1$ Ly α LFs, because our $z = 2.2$ Ly α LF is derived in the same manner as Ouchi et al. (2008) based on the similar Subaru narrowband data (Sections 3.2–3.4).

We extend our investigation of Ly α LF evolution from $z = 2 - 3$ to $z = 0 - 6$. The left panel of Figure 6 compares our best-estimate Ly α LF at $z = 2.2$ with the Ly α LFs at $z = 0.3, 0.9, 3.1, 3.7$, and 5.7 taken from the literature. The right panel of Figure 6 shows the error contours of our Schechter function fitting, where we fix the α value to our best-fit slope $\alpha = -1.8$ of our $z = 2.2$ Ly α LF. The Ly α LFs at $z = 0.3$ and 0.9 are derived by the spectroscopic surveys with the *GALEX* FUV and NUV grism data, respectively (Cowie et al. 2010; Barger et al. 2012). We show the Ly α LF measurements at

$z = 3.7$ and 5.7 given by Ouchi et al. (2008). We summarize the best-fit Schechter parameters at $z = 0 - 6$ in Table 5. Note that EW $_0$ limits for the selection of LAEs are EW $_0 \gtrsim 10 - 30 \text{ \AA}$ for all of the samples listed in Table 5 except for those of Ouchi et al.’s $z = 3.1$ and 3.7 samples and our EW > 60 sample. In the right panel of Figure 6, there is a significant increase of Ly α LFs in $L_{\text{Ly}\alpha}^*$ and/or $\phi_{\text{Ly}\alpha}^*$ from $z \sim 0$ to 3 , albeit with the uncertain decrease of $\phi_{\text{Ly}\alpha}^*$ from $z = 0.3$ to 0.9 , which is first claimed by Deharveng et al. (2008). The right panel of Figure 6 also suggests no significant evolution of the Ly α LFs at $z = 3 - 6$ that is concluded by Ouchi et al. (2008).

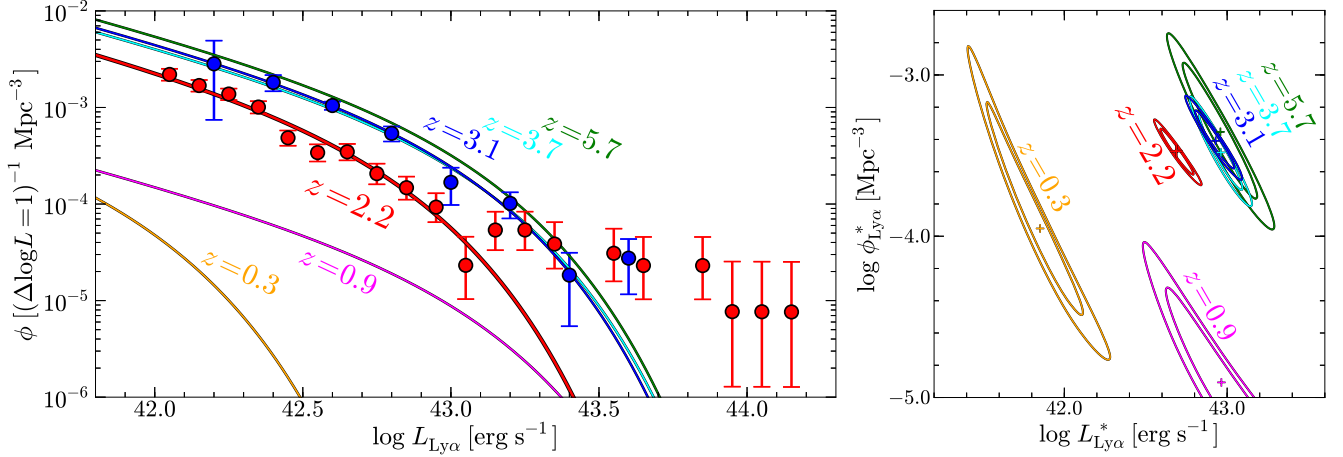


Figure 6. *Left:* Evolution of Ly α LF from $z = 0$ to 6. The red filled circles are our $z = 2.2$ Ly α LF of the EW > 60 sample, and the blue filled circles denote the LF at $z = 3.1$ derived by Ouchi et al. (2008). The orange, magenta, red, blue, cyan, and green curves show the best-fit Schechter functions of the Ly α LFs at $z = 0.3$ (Cowie et al. 2010), 0.9 (Barger et al. 2012), 2.2 (this work), 3.1, 3.7, and 5.7 (Ouchi et al. 2008), respectively. These Schechter functions are derived with a fixed slope value of $\alpha = -1.8$ that is the best-fit value of our $z = 2.2$ Ly α LF. *Right:* Error contours of Schechter parameters, $L_{\text{Ly}\alpha}^*$ and $\phi_{\text{Ly}\alpha}^*$. The orange, magenta, red, blue, cyan, and green contours represent the error contours of the Schechter parameters at $z = 0.3, 0.9, 2.2, 3.1, 3.7$, and 5.7, respectively. The inner and outer contours indicate the 68% and 90% confidence levels, respectively.

Table 5
Best-fit Schechter Parameters and Ly α Luminosity Densities

Redshift	$L_{\text{Ly}\alpha}^*$ (10^{42} erg s $^{-1}$)	$\phi_{\text{Ly}\alpha}^*$ (10^{-4} Mpc $^{-3}$)	$\rho_{\text{Ly}\alpha\text{obs}}^a$ (10^{39} erg s $^{-1}$ Mpc $^{-3}$)	Reference
0.3	$0.71^{+0.32}_{-0.29}$	$1.12^{+2.45}_{-0.61}$	$0.055^{+0.019}_{-0.014}$	Cowie et al. (2010)
0.9	$9.22^{+15.6}_{-3.80}$	$0.12^{+0.18}_{-0.09}$	$0.165^{+0.067}_{-0.050}$	Barger et al. (2012)
2.2	$5.29^{+1.67}_{-1.13}$	$6.32^{+3.08}_{-2.31}$	$5.93^{+0.23}_{-0.22}$	This work (Best estimate)
2.2	$4.87^{+0.83}_{-0.68}$	$3.37^{+0.80}_{-0.66}$	$2.17^{+0.13}_{-0.13}$	This work (EW > 60 sample)
3.1	$8.49^{+1.65}_{-1.46}$	$3.90^{+1.27}_{-0.90}$	$4.74^{+0.46}_{-0.42}$	Ouchi et al. (2008)
3.7	$9.16^{+2.03}_{-1.67}$	$3.31^{+1.42}_{-0.98}$	$4.36^{+0.73}_{-0.63}$	Ouchi et al. (2008)
5.7	$9.09^{+3.67}_{-2.70}$	$4.44^{+4.04}_{-2.05}$	$5.81^{+1.87}_{-1.43}$	Ouchi et al. (2008)
6.6	$6.69^{+2.51}_{-1.62}$	$4.17^{+2.70}_{-1.72}$	$3.86^{+0.86}_{-0.70}$	Ouchi et al. (2010)
7.3	$3.23^{+25.0}_{-1.63}$	$2.82^{+17.6}_{-2.70}$	$1.12^{+2.30}_{-0.68}$	Konno et al. (2014)

Note. — For $z = 2.2$ (Best estimate), the best-fit Schechter parameters are determined with the full sample (Section 3.4), while for the other cases, $L_{\text{Ly}\alpha}^*$ and $\phi_{\text{Ly}\alpha}^*$ are derived with a fixed value of $\alpha = -1.8$, which is consistent with the best-fit value for our Ly α LF at $z = 2.2$. Note that EW $_0$ limits for the selection of LAEs at $z = 0.3, 0.9, 2.2$ (Best estimate), 2.2 (EW > 60 sample), 3.1, 3.7, 5.7, 6.6, and 7.3 are EW $_0 = 15, 20, \sim 20 - 30, 60, \sim 60, \sim 40, \sim 30, \sim 10$, and ~ 0 , respectively.

^a Ly α luminosity densities obtained by integrating the Ly α LF down to $\log L_{\text{Ly}\alpha} = 41.41$ erg s $^{-1}$.

4.2. Ly α Luminosity Density Evolution

We calculate the Ly α luminosity densities (LDs),

$$\rho_{\text{obs}}^{\text{Ly}\alpha} = \int_{L_{\text{lim}}^{\text{Ly}\alpha}}^{\infty} L_{\text{Ly}\alpha} \phi_{\text{Ly}\alpha}(L_{\text{Ly}\alpha}) dL_{\text{Ly}\alpha}, \quad (9)$$

at $z = 0 - 8$ with the Ly α LFs shown in Section 4.1, where $L_{\text{lim}}^{\text{Ly}\alpha}$ is the Ly α luminosity limit for the Ly α LD estimates. We choose the common Ly α luminosity limit of $\log L_{\text{lim}}^{\text{Ly}\alpha} = 41.41$ erg s $^{-1}$ that corresponds to $0.03 L_{\text{Ly}\alpha, z=3}^*$.

There are two systematic uncertainties for estimates of the Ly α LDs. One uncertainty is the choice of Ly α luminosity limits. The Ly α luminosity limit can be lower than $\log L_{\text{lim}}^{\text{Ly}\alpha} = 41.41$ erg s $^{-1}$ to estimate representative Ly α LDs. However, we confirm that the estimated Ly α LDs are not largely different even if we integrate the Ly α LFs down to a fainter luminosity of $\log L_{\text{Ly}\alpha} = 40.0$ erg s $^{-1}$. The largest

Ly α LD difference of ~ 0.4 dex is found at $z = 0.3$, because the $L_{\text{Ly}\alpha}^*$ value at $z = 0.3$ is significantly smaller than those at the other redshifts. Another uncertainty is Ly α EW limits for selection of LAEs. Ly α LDs are based on LAE samples selected with a Ly α EW limit (i.e., EW $_0 \gtrsim 10 - 30 \text{ \AA}$). Ouchi et al. (2008) estimate Ly α LDs for all (EW > 0 \AA) LAEs and find that the Ly α LDs are slightly larger than those for their EW-limited LAE samples (EW $_0 \gtrsim 10 - 30 \text{ \AA}$) by ~ 0.1 dex at most. These levels of differences do not change the results of the Ly α LD evolution in this Section that is at the level of an order of magnitude. For these Ly α LDs, we do not correct the Ly α flux attenuation by neutral hydrogen (H I) in the IGM. The Ly α LDs represent the amount of Ly α photons escaping not only from ISM of galaxies, but also from the H I IGM.

For comparison, we also use UV LDs taken from the liter-

ature (Bouwens et al. 2015). The UV LD is defined by

$$\rho_{\text{obs}}^{\text{UV}} = \int_{L_{\text{lim}}^{\text{UV}}}^{\infty} L_{\text{UV}} \phi_{\text{UV}}(L_{\text{UV}}) dL_{\text{UV}}, \quad (10)$$

where $L_{\text{lim}}^{\text{UV}}$ is the UV luminosity limit for the UV LD estimates, and $\phi_{\text{UV}}(L_{\text{UV}})$ is the best-fit Schechter function for the UV LF measurements. Here, the value of $L_{\text{lim}}^{\text{UV}}$ is $0.03L_{\text{UV},z=3}^*$ ($M_{\text{UV}} = -17.0$ mag). The upper panel of Figure 7 presents the evolution of the Ly α LDs as a function of redshift whose data are summarized in Table 5. In the upper panel of Figure 7, we also plot the UV LDs of dust-uncorrected and -corrected UV LDs obtained by Bouwens et al. (2015). Similar to the evolutionary trends of Ly α LFs described in Section 4.1, we find the significant increase of Ly α LDs from $z \sim 2$ to 3 beyond the measurement errors. Moreover, there is a rapid increase of Ly α LDs by nearly two order of magnitudes from $z \sim 0$ to 3, and a plateau of Ly α LDs between $z \sim 3$ and 6. The decrease of Ly α LDs at $z \gtrsim 6$ is also found. For more details, see Section 4.1 and the literature (e.g. Deharveng et al. 2008; Ouchi et al. 2008; Cowie et al. 2010, 2011; Ciardullo et al. 2012; Barger et al. 2012; Wold et al. 2014; Konno et al. 2014).

The Ly α LD evolution is different from the UV LD evolution in the upper panel of Figure 7. There is an increase of UV LDs from $z \sim 0$ to 3, but the increase is only about an order of magnitude that is not as large as the one of Ly α LDs. At $z \sim 3 - 6$, the UV LDs show a moderate decrease and no evolutionary plateau like the one found in the Ly α LD evolution. At $z \gtrsim 6$, the decrease of Ly α LDs is faster than the one of UV LDs toward high- z . We discuss the physical origins of these differences in Section 5.3.

5. DISCUSSION

5.1. Bright-End Hump of the Ly α LF

In the upper panel of Figure 3, we find the bright-end hump of our $z = 2.2$ Ly α LF at $\log L_{\text{Ly}\alpha} \gtrsim 43.4$ erg s $^{-1}$. The objects in the bright-end hump have UV continuum magnitudes of $M_{\text{UV}} \gtrsim -25$. There are two possibilities to explain this hump. One possibility is the existence of AGNs which have a strong Ly α emission line (e.g., Ouchi et al. 2008). Another possibility is the magnification bias (e.g., Wyithe et al. 2011; Mason et al. 2015). The gravitational lensing of foreground massive galaxies increases luminosities of LAEs at $z = 2.2$ that make the hump at the bright end LF. The lower panel of Figure 3 shows that all galaxies brighter than $\log L_{\text{Ly}\alpha} = 43.4$ erg s $^{-1}$ have (a) bright counterpart(s) in X-ray, UV, and/or radio data, suggesting that these galaxies have AGNs. If we remove these galaxies from our sample, the shape of the Ly α LF is explained by the simple Schechter function with no hump (see the black solid line and black filled circles in the lower panel of Figure 3). These results indicate that the bright-end hump is almost fully explained by AGNs that have magnitudes of $M_{\text{UV}} \gtrsim -25$. These AGNs are significantly fainter than QSOs, and regarded as faint AGNs. The magnification bias would exist, but it is very weak. The major physical mechanism of the bright-end hump is not the magnification bias.

5.2. Faint AGN UV LF

In Section 5.1, we discuss that the bright-end hump is made of faint AGNs ($\log L_{\text{Ly}\alpha} > 43.4$ erg s $^{-1}$), all of which have the counterpart(s) in the X-ray, UV, and radio data. Using the

abundance and the UV continuum magnitudes ($M_{\text{UV}} \gtrsim -25$) of these faint AGNs, we derive faint AGN UV LFs. These faint AGN UV LFs complement the bright AGN UV LFs obtained by cosmological large scale surveys such as Sloan Digital Sky Survey (SDSS). To estimate the faint AGN UV LFs, we measure i -band magnitudes at the positions of the faint AGNs. Here, we choose the i -band magnitudes for UV continuum magnitude estimates, because we compare our results with the SDSS AGN study of Ross et al. (2013) who use i -band magnitudes to derive their AGN UV LF. All of our faint AGNs are detected at the $> 5\sigma$ levels in our i -band images. Note that the 5σ limiting magnitudes of our i -band images correspond to $M_{\text{UV}} = -17.9, -18.6, -20.2, -19.7$, and -18.5 mag for the faint AGNs at $z = 2.2$ in the SXDS, COSMOS, CDFS, HDFN, and SSA22 fields, respectively. We calculate the volume number densities of the faint AGNs in a UV-continuum magnitude bin, dividing the number counts of faint AGNs by our comoving survey volume ($\simeq 1.32 \times 10^6$ Mpc 3). Figure 8 presents these UV LFs of our faint AGNs with black open circles that we call raw UV LFs. The errors of the raw UV LFs are the Poisson errors for small number statistics (Gehrels 1986).

Because AGNs do not always have Ly α emission that can be identified by our narrowband observations, the raw UV LFs are incomplete. The raw UV LFs are regarded as the lower limits of the AGN UV LFs. To evaluate the incompleteness, we use the relation of Ly α EWs and UV-continuum magnitudes given by Dietrich et al. (2002). Dietrich et al. (2002) obtain the median values of Ly α EWs at a given UV-continuum magnitude bin based on 744 AGNs at $z \sim 0 - 5$, where a negligibly small fraction ($\sim 10\%$) of damped Ly α systems and low quality data is removed from their AGN sample. In Figure 9, we plot the median values with the black filled diamonds. Because no PDFs of Ly α EWs are presented in Dietrich et al. (2002), the errors of the black filled diamonds represent the measurement uncertainties of Ly α EWs. Figure 9 shows a correlation, indicating that UV-continuum faint AGNs have large Ly α EWs. The red and blue lines in Figure 9 represent our selection limits of $\log L_{\text{Ly}\alpha} > 43.4$ erg s $^{-1}$ (for the objects in the bright-end hump) and the $\text{EW}_0 \gtrsim 20 - 30 \text{ \AA}$ (for our LAE sample), respectively. In Figure 9, we find that these selection limits (red and blue lines) are far below the median values (black diamonds) at $M_{\text{UV}} \lesssim -22.5$. Thus, the faint AGN UV LFs at $M_{\text{UV}} \lesssim -22.5$ can be determined with reasonable completeness corrections. Because the Ly α EW PDFs are not given in Dietrich et al. (2002), one cannot simply estimate the incompleteness. However, all of the median values at $M_{\text{UV}} \lesssim -22.5$ are placed above the selection limits. The maximum correction factor is ~ 2 in the most extreme case that the Ly α EW PDF has the bottom heavy distribution. This is because about a half of the AGNs at maximum could fall below our selection limits, which can keep the median values as high as those obtained by Dietrich et al. (2002). For our faint AGNs at $M_{\text{UV}} \lesssim -22.5$, we correct the raw UV LFs for the incompleteness with the maximum correction factor, and plot the maximally-corrected UV LFs with the open squares in Figure 8. Because the real UV LFs should be placed between the raw UV LFs and the maximally-corrected UV LFs, we define the best-estimate UV LFs by the average of the raw and maximally-corrected UV LFs with the conservative error bars that completely cover the 1σ uncertainties of these two UV LFs. The red circles in Figure 8 represent the best-estimate UV LFs. In Figure 8, we also present

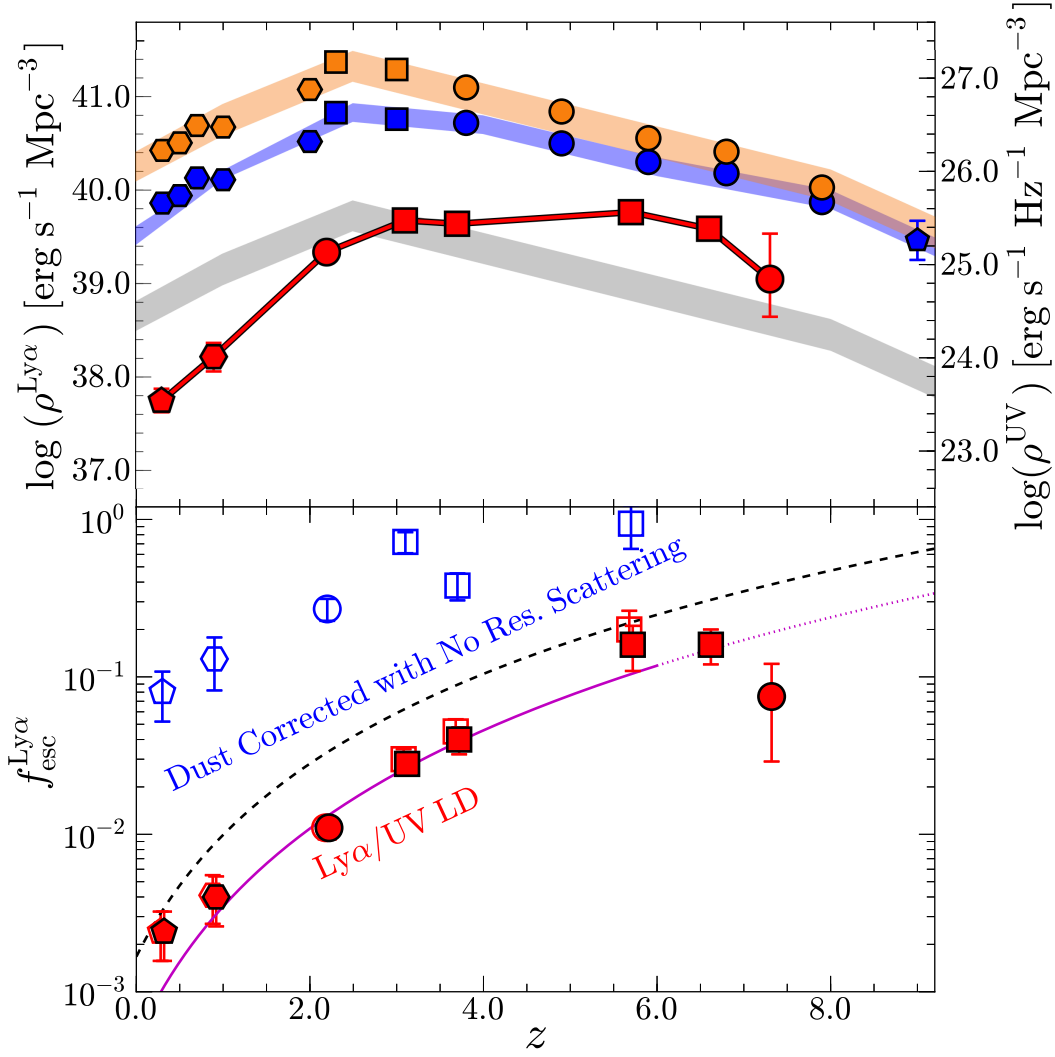


Figure 7. *Top:* Evolution of Ly α LDs and UV LDs as a function of redshift. The red circle at $z = 2.2$ shows the Ly α LD obtained by this study. The red pentagon at $z = 0.3$ and hexagon at $z = 0.9$ are the Ly α LDs derived by Cowie et al. (2010) and Barger et al. (2012), respectively. The red squares at $z = 3.1, 3.7, 5.7$, and 6.6 denote the results of Ouchi et al. (2008, 2010), and the red circle at $z = 7.3$ is the measurement given by Konno et al. (2014). The blue symbols and shaded area represent the evolution of the dust-uncorrected UV LDs. The blue pentagons at $z = 0 - 2$ and squares at $z = 2 - 3$ are the UV LDs obtained by Schiminovich et al. (2005) and Reddy & Steidel (2009), respectively. The blue circles and pentagon show the UV LDs given by Bouwens et al. (2015) for $z = 3.8, 4.9, 5.9, 6.8$, and 7.9 , and Ellis et al. (2013) for $z = 9.0$, respectively. The orange symbols and shaded area are the same as the blue ones, but for the dust-corrected UV LDs. The gray shaded area denotes the evolutionary tendency of the dust-corrected UV LDs scaled to the Ly α LD at $z \sim 3$ for comparison.

Bottom: Evolution of Ly α escape fraction, $f_{\text{esc}}^{\text{Ly}\alpha}$, as a function of redshift. The red filled symbols show the Ly α escape fractions derived from the observed Ly α LDs and dust-corrected UV LDs (Equation 12). The red open symbols represent our Ly α escape fraction values corrected for IGM absorption using the relation of Madau (1995). The blue open symbols indicate the Ly α escape fractions corrected for dust extinction in the case of no Ly α resonance scattering (Equation 16). The magenta solid line is the best-fit function for our Ly α escape fraction evolution from $z = 0$ to 6 ($f_{\text{esc}}^{\text{Ly}\alpha} = 5.0 \times 10^{-4} \times (1+z)^{2.8}$), while the black dashed line is the best-fit function derived by Hayes et al. (2011). The magenta dotted line represents the extrapolation of the magenta solid line to $z > 6$.

the AGN UV LFs at $z \sim 2.2$ derived with the SDSS DR9 data (the blue circles; Ross et al. 2013) and the 2dF-SDSS LRG and QSO survey data (the green circles; Croom et al. 2009). There is a magnitude-range overlap of our, Ross et al.'s, and Croom et al.'s AGN UV LF estimates at $M_{\text{UV}} \simeq -24.8$. The number densities from our, Ross et al.'s, and Croom et al.'s studies agree very well within the uncertainties at the overlap magnitude, indicating that our AGN UV LF estimates are reliable.

We fit a double power-law function to the AGN UV LFs of ours, Ross et al. (2013), and Croom et al. (2009). The double power-law function for the AGN number density,

$\phi_{\text{AGN}}(M_{\text{UV}})$, is defined by

$$\phi_{\text{AGN}}(M_{\text{UV}}) = \frac{\phi_{\text{AGN}}^*}{10^{0.4(\alpha_{\text{AGN}}+1)(M_{\text{UV}}-M_{\text{AGN}}^*)} + 10^{0.4(\beta_{\text{AGN}}+1)(M_{\text{UV}}-M_{\text{AGN}}^*)}}, \quad (11)$$

where ϕ_{AGN}^* and M_{AGN}^* are the characteristic number density and magnitude of AGNs, respectively. The parameters of α_{AGN} and β_{AGN} determine the faint- and bright-end slopes of the AGN UV LFs. We obtain the best-fit parameters of $\phi_{\text{AGN}}^* = 1.8 \pm 0.2 \times 10^{-6} \text{ Mpc}^{-3}$, $M_{\text{AGN}}^* = -26.2 \pm 0.1$, $\alpha_{\text{AGN}} = -1.2 \pm 0.1$, and $\beta_{\text{AGN}} = -3.3 \pm 0.1$, and present the best-fit function with the red line in Figure 8. Our results

suggest that the faint-end slope α_{AGN} is moderately flat at $M_{\text{UV}} \simeq -23$ to -25 .

Ross et al. (2013) and Croom et al. (2009) show the faint-end slopes at $z \sim 2.2$ are $\alpha_{\text{AGN}} = -1.3^{+0.7}_{-0.1}$ and -1.4 ± 0.2 , respectively, that are consistent with our result. Because relatively steep faint-end slopes ($\alpha_{\text{AGN}} \simeq -1.5$ to -1.8) are obtained for $z = 4$ to 6.5 AGNs (Ikeda et al. 2011; Giallongo et al. 2015), our moderately flat faint-end slope at $z \sim 2.2$ would suggest that the faint-end slope steepens toward high- z . Figure 8 displays the two models of a pure luminosity evolution (PLE) model and a luminosity evolution and density evolution (LEDE) model that are introduced by Ross et al. (2013). Comparing these two models, we find that the LEDE model explains our AGN UV LFs better than the PLE model. This comparison suggests that the AGN UV LF evolution involves both luminosities and densities.

5.3. Ly α Escape Fraction Evolution and the Physical Origins

In Section 4.2, we compare the evolution of the Ly α and UV LDs, and conclude that the evolutions of Ly α and UV LDs are different. To understand the physical origins of the differences between Ly α and UV LD evolutions, we investigate evolution of Ly α escape fractions, $f_{\text{esc}}^{\text{Ly}\alpha}$. The Ly α escape fraction evolution is investigated by previous studies (e.g., Hayes et al. 2011; Blanc et al. 2011). In this study, we revisit the Ly α escape fraction evolution, because there are significant progresses on the estimates of Ly α LDs from recent Subaru, VLT, and HETDEX pilot surveys (e.g., Cassata et al. 2011; Ciardullo et al. 2014; Konno et al. 2014) and UV LDs from HST UDF12, CANDELS, and HFF programs (e.g., Bouwens et al. 2015).

The Ly α escape fraction is defined by

$$f_{\text{esc}}^{\text{Ly}\alpha} = \rho_{\text{SFRD}}^{\text{obs, Ly}\alpha} / \rho_{\text{SFRD}}^{\text{int, UV}}, \quad (12)$$

where $\rho_{\text{SFRD}}^{\text{obs, Ly}\alpha}$ is the star formation rate densities (SFRDs) estimated from the observed Ly α LDs. The variable of $\rho_{\text{SFRD}}^{\text{int, UV}}$ represents SFRDs calculated from the intrinsic UV LDs that are UV LDs corrected for dust extinction. Note that the contribution from AGN luminosities to Ly α LDs and UV LDs are negligibly small due to the low AGN abundance, and that we regard these Ly α and UV photons are produced by star formation.

We use the Ly α LDs shown in Figure 7 (Section 4.2), and derive $\rho_{\text{SFRD}}^{\text{obs, Ly}\alpha}$. In the estimation of star-formation rates (SFRs) from the Ly α luminosities, we apply

$$\text{SFR} (M_{\odot} \text{ yr}^{-1}) = L_{\text{Ly}\alpha} (\text{erg s}^{-1}) / (1.1 \times 10^{42}), \quad (13)$$

that is the combination of the H α luminosity-SFR relation (Kennicutt 1998) and the case B approximation (Brocklehurst 1971). For $\rho_{\text{SFRD}}^{\text{int, UV}}$ values, we use the dust-extinction corrected SFRDs derived by Bouwens et al. (2015). The SFRDs are estimated from the UV LDs that are integrated values of UV LFs down to $0.03 L_{\text{UV}, z=3}^*$ (Section 4.2). The SFRs are estimated from UV luminosities with the equation (Madau et al. 1998),

$$\text{SFR} (M_{\odot} \text{ yr}^{-1}) = L_{\text{UV}} (\text{erg s}^{-1} \text{ Hz}^{-1}) / (8 \times 10^{27}), \quad (14)$$

where L_{UV} is the UV luminosity measured at 1500 Å. The dust extinction values are evaluated from the UV-continuum slope measurements with the relation of Meurer et al. (1999).

The UV LDs corresponding to these SFRDs are presented in Figure 7. Note that the Salpeter IMF is assumed in Equations (13) and (14).

From these SFRDs, we estimate Ly α escape fractions with Equation (12). The bottom panel of Figure 7 presents the Ly α escape fractions at $z \sim 0$ to 8 . We fit a power-law function of $\propto (1+z)^n$ to these Ly α escape fraction estimates at $z \sim 0$ to 6 , where n is the power law index. We obtain the best-fit function of $f_{\text{esc}}^{\text{Ly}\alpha} = 5.0 \times 10^{-4} \times (1+z)^{2.8}$. The best-fit function is shown in the bottom panel of Figure 7. The best-fit function indicates a large increase of Ly α escape fractions from $z \sim 0$ to 6 by two orders of magnitude, although the data points of $z \gtrsim 6$ depart from the best-fit function. This trend is similar to the one claimed by Hayes et al. (2011). We compare the results of Hayes et al. (2011) with this study in the bottom panel of Figure 7. Although the general evolutionary trend is the same in Hayes et al.'s and our results, there is a small offset between these two results. This offset is explained by the differences of the Ly α and UV luminosity limits for deriving the Ly α and UV LDs from Ly α and UV LFs, respectively. In fact, we obtain Ly α escape fractions consistent with those of Hayes et al. (2011), if we calculate the Ly α escape fractions with the Ly α and UV luminosity limits same as those of Hayes et al. (2011). In other words, the choice of Ly α and UV luminosity limits moderately change the Ly α escape fraction estimates, but the two-orders of magnitude evolution of Ly α escape fractions is significantly larger than these changes.

At $z \gtrsim 6$, there exist the departures of the Ly α escape fraction estimates from the best-fit function (the bottom panel of Figure 7). Moreover, the departure becomes larger toward high- z . There is a decrease of Ly α escape fractions from $z \sim 6$ to 8 by a factor of ~ 2 . Because the redshift range of $z \gtrsim 6$ corresponds to the epoch of reionization (EoR), this decrease of Ly α escape fractions at $z \gtrsim 6$ is explained by the increase of Ly α scattering of H I in the IGM at the EoR. In other words, it is likely that the physical origin of the $f_{\text{esc}}^{\text{Ly}\alpha}$ decrease at $z \gtrsim 6$ is cosmic reionization. This result is in the different form of the previous results that claim the signature of cosmic reionization based on the Ly α luminosity function decrease at $z > 6$ (e.g. Kashikawa et al. 2006; Ouchi et al. 2010; Kashikawa et al. 2011; Shibuya et al. 2012; Konno et al. 2014) and the Ly α -emitting galaxy fraction decrease at $z > 6$ (e.g. Pentericci et al. 2011; Ono et al. 2012; Treu et al. 2013; Schenker et al. 2014).

Here, we discuss the physical mechanism of the large, two orders of magnitude increase of $f_{\text{esc}}^{\text{Ly}\alpha}$ from $z \sim 0$ to 6 . Note that $f_{\text{esc}}^{\text{Ly}\alpha}$ is defined as the ratio of the Ly α LD to the UV LD of star-forming galaxies. Since these LDs are mainly contributed by continuum faint galaxies with $M_{\text{UV}} \gtrsim -19$, majority of which show Ly α in emission (Stark et al. 2010), we regard LAEs as a dominant population of high- z star-forming galaxies in the following discussion.

There are four possible physical mechanisms for the large $f_{\text{esc}}^{\text{Ly}\alpha}$ increase from $z \sim 0$ to 6 : evolutions of stellar population, outflow, dust extinction, and Ly α scattering of H I in the galaxy's ISM. It should be noted that the IGM absorption of Ly α becomes strong from $z \sim 0$ to 6 , and that the evolution of IGM absorption suppresses $f_{\text{esc}}^{\text{Ly}\alpha}$ (see below for the quantitative arguments), which cannot be a physical mechanism for the $f_{\text{esc}}^{\text{Ly}\alpha}$ increase towards high- z . For the possibility of stellar population evolution, the estimates of the $f_{\text{esc}}^{\text{Ly}\alpha}$ would increase, if more ionizing photons for a given SFR are produced in galaxies that have very massive stars

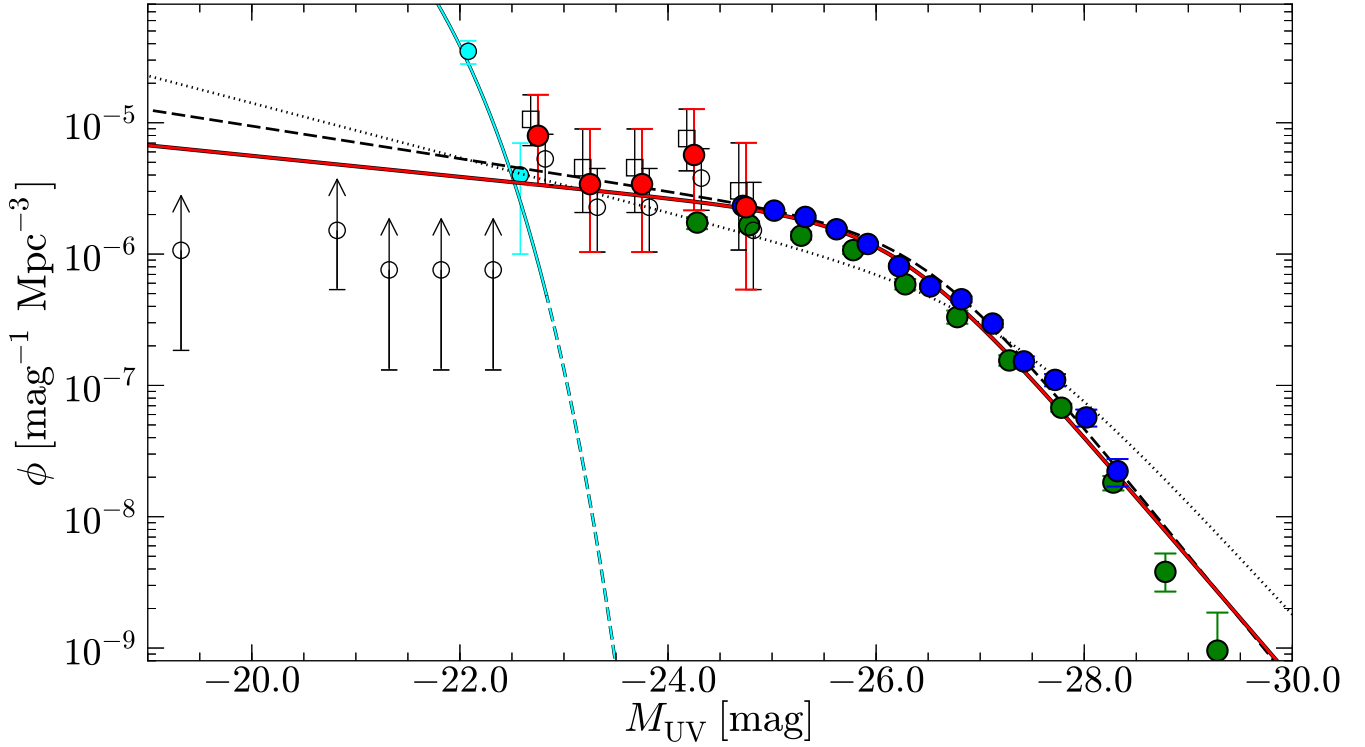


Figure 8. UV LF of faint AGNs. The red filled circles denote the best-estimate AGN UV LFs and the black open circles and squares represent the raw and maximally-corrected AGN UV LFs, respectively (see the text for details). At $M_{UV} \gtrsim -22.5$, we plot only the raw UV LF as lower limits with black arrows, because one cannot estimate the incompleteness at this range (see the text for details). For display purposes, we slightly shift the black symbols along the abscissa. The blue and green circles are the AGN UV LFs at $z \sim 2.2$ derived from the SDSS DR9 dataset (Ross et al. 2013) and the 2dF-SDSS LRG and QSO survey dataset (Croom et al. 2009), respectively. The red curve shows the best-fit function for the AGN UV LFs of ours, Ross et al. (2013), and Croom et al. (2009). The black dotted and dashed curves represent the best-fit functions under the assumptions of the PLE and LEDE models introduced by Ross et al. (2013), respectively. We also display the UV LF of $z = 2$ LBGs obtained by Reddy & Steidel (2009) with the cyan circles. The cyan solid curve represents the best-fit Schechter function of the LBG UV LF within a range of the observed UV-continuum magnitude (i.e., $M_{UV} > -22.8$), while the cyan dashed curve denotes the function extrapolated to $M_{UV} < -22.8$.

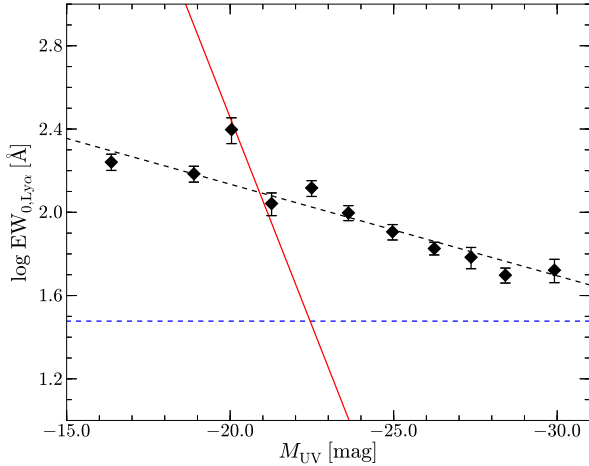


Figure 9. $\text{Ly}\alpha$ EW_0 as a function of UV-continuum magnitude of AGN. The black diamonds represent the median values of the observed $\text{Ly}\alpha$ EW_0 at a given UV-continuum magnitude, and the black dashed line is a best-fit linear function obtained by Dietrich et al. (2002). The error bars of the black diamonds indicate the measurement uncertainties of the $\text{Ly}\alpha$ EWs. The red solid line shows a locus of the luminosity for $\log L_{\text{Ly}\alpha} = 43.4$ erg s^{-1} , which is a selection criterion for our faint AGNs. The blue dashed line denotes the EW_0 threshold for selection of our $z = 2.2$ LAEs (i.e., $\sim 20 - 30$ Å).

found in the early stage of star-formation. However, the average/median stellar ages of LAEs for a constant star-formation

history are 10 – 300 Myr at $z = 2 - 6$ (c.g., Gawiser et al. 2006; Pirzkal et al. 2007; Lai et al. 2008; Ono et al. 2010a,b; Guaita et al. 2011), which are comparable with those at $z \sim 0$ (e.g., Cowie et al. 2011; Hayes et al. 2014). Because there are no systematic differences in stellar ages by redshift, the difference of stellar population does not explain the large increase of $f_{\text{esc}}^{\text{Ly}\alpha}$. For the possibility of outflow, it is likely that gas outflow of galaxies help $\text{Ly}\alpha$ photons escape from the ISM, because the $\text{Ly}\alpha$ resonance wavelength of the ISM is redshifted by the bulk gas motion of outflow. If there is a systematic difference in outflow velocities, the $f_{\text{esc}}^{\text{Ly}\alpha}$ values change. Because the typical outflow velocities of LAEs are 50 – 200 km s^{-1} that show no systematic change over the redshift range of $z \sim 0 - 6$ (Hashimoto et al. 2013; Wofford et al. 2013; Erb et al. 2014; Shibuya et al. 2014; Stark et al. 2015; Rivera-Thorsen et al. 2015)⁶, the galaxy outflow would not be a major reason of the large $f_{\text{esc}}^{\text{Ly}\alpha}$ increase. For the possibility of dust extinction evolution, it is thought that the amount of dust in galaxies decreases from $z \sim 0$ to 6, and that galaxies with small dust extinction have large $f_{\text{esc}}^{\text{Ly}\alpha}$ values. Because the dust attenuation of $\text{Ly}\alpha$ is enhanced by the resonance scat-

⁶ These outflow velocity measurements are obtained for UV-continuum bright galaxies, except for a few lensed galaxies. Because the outflow velocities of LAEs are similar to those of LBGs (150–200 km s^{-1} ; e.g., Hashimoto et al. 2013; Erb et al. 2014; Shibuya et al. 2014), UV-continuum faint galaxies would have the outflow velocity comparable to that of UV-bright galaxies.

tering of H I in the galaxy's ISM that depends on the H I density, we first obtain crude estimates of dust extinction effects with no resonance scattering. We estimate the luminosity averaged stellar extinction, $E(B - V)_*$, from the dust-corrected and uncorrected UV LDs by the equation,

$$\rho_{\text{SFRD}}^{\text{int,UV}} = 10^{0.4 \times E(B-V)_* \times k_{\text{UV}}} \times \rho_{\text{SFRD}}^{\text{uncorr,UV}}, \quad (15)$$

where $\rho_{\text{SFRD}}^{\text{uncorr,UV}}$ is the dust-uncorrected UV SFRDs (Section 4.2) calculated with Equation (14). The value of k_{UV} is the extinction coefficient at 1500 Å, which is derived with the Calzetti's extinction law (Calzetti et al. 2000), $k_{\text{UV}} = 10.3$. We thus obtain $E(B - V)_*$ values over $z \sim 0 - 6$. From these $E(B - V)_*$ values, we estimate $f_{\text{esc,dust}}^{\text{Ly}\alpha}$ with

$$f_{\text{esc,dust}}^{\text{Ly}\alpha} = 10^{-0.4 \times k_{1216} \times E(B-V)_{\text{gas}}}, \quad (16)$$

where k_{1216} is the extinction coefficient at 1216 Å, $k_{1216} = 12.0$, estimated with the Calzetti et al.'s law. Here we adopt $E(B - V)_{\text{gas}} = E(B - V)_* / 0.44$ (Calzetti et al. 2000). The blue open symbols in Figure 7 present the Ly α escape fraction values corrected for dust extinction, $f_{\text{esc}}^{\text{Ly}\alpha} / f_{\text{esc,dust}}^{\text{Ly}\alpha}$, in the case of no resonance scattering. The dust-corrected Ly α escape fractions are nearly unity at $z \sim 6$, while these fractions significantly drop from $z \sim 4$ to $z \sim 0$. At $z \sim 0$, the dust-corrected Ly α escape fraction is about an order of magnitude smaller than unity. There is a clear redshift dependence. We find that the large fraction of Ly α escape fraction evolution can be partly explained by dust extinction with no resonance scattering, but that there still remains the large discrepancy at $z < 4$. Thus, the large $f_{\text{esc}}^{\text{Ly}\alpha}$ evolution requires the evolution of Ly α scattering of H I in the galaxy's ISM from $z \sim 0$ to 6 that enhances the dust attenuation. Due to the resonance nature of the Ly α line, an increase of the H I density provides longer path lengths that strengthen the effects of the ISM scattering with a small amount of dust. Indeed, several studies suggest that the high H I density of star-forming galaxies largely scatter Ly α photons (Shapley et al. 2003; Pentericci et al. 2007; Verhamme et al. 2008; Atek et al. 2009; Pardy et al. 2014).

Here, we estimate the H I column density, N_{HI} , of ISM that needs to explain the large $f_{\text{esc}}^{\text{Ly}\alpha}$ increase from $z \sim 0$ to 6 with the non-resonant extinction values obtained by the observational data. We use the 3D Ly α Monte-Carlo radiative transfer code, MCLya of Verhamme et al. (2006) and Schaerer et al. (2011). The MCLya code computes the Ly α radiative transfer in an expanding homogeneous shell of ISM H I and dust that surrounds a central Ly α source. The dust extinction effects are self-consistently calculated for the resonance line of Ly α . The MCLya code has four physical parameters to describe the physical properties of the shell: N_{HI} , the nebular dust extinction $E(B - V)_{\text{gas}}$, the radial expansion velocity v_{exp} , and the Doppler parameter b that includes both thermal and turbulent gas motions within the shell. At each redshift shown in Figure 7, we derive the best-estimate N_{HI} value, using the $E(B - V)_{\text{gas}}$ values obtained above. We set $b = 12.8$ km s $^{-1}$ that is a fiducial value, although the b parameter negligibly changes our results. For v_{exp} , we adopt the average outflow velocity of galaxies at $z \sim 0 - 6$, $v_{\text{exp}} = 150$ km s $^{-1}$ (Jones et al. 2012; Hashimoto et al. 2013; Shibuya et al. 2014; Stark et al. 2015; Rivera-Thorsen et al. 2015). Because the outflow velocity measurements, available to date, have large uncertainties, we allow the moderately large range of

outflow velocities, $v_{\text{exp}} = 50 - 200$ km s $^{-1}$, that includes most of outflow velocity measurements for the low- z and high- z LAEs and LBGs so far obtained (Jones et al. 2012; Hashimoto et al. 2013; Shibuya et al. 2014; Stark et al. 2015; Rivera-Thorsen et al. 2015).

We obtain the best-estimate N_{HI} values with the three fixed parameters for the MCLya code, calculating the Ly α escape fractions that agrees with those of the observational estimates. For the observational estimates of the Ly α escape fractions, we use the Ly α escape fraction that is corrected for the IGM absorption, $f_{\text{esc}}^{\text{Ly}\alpha} / f_{\text{esc,IGM}}^{\text{Ly}\alpha}$ (red open symbols in the bottom panel of Figure 7), where $f_{\text{esc,IGM}}^{\text{Ly}\alpha}$ is the Ly α escape fraction contributed only by the IGM H I Ly α absorption. We estimate $f_{\text{esc,IGM}}^{\text{Ly}\alpha}$ with the formalism of Madau (1995), assuming no effects of Ly α dumping wing absorption that is negligible in the redshift range of $z = 0 - 6$ after the cosmic reionization. In Figure 10, we show the best-estimate N_{HI} values for the average outflow velocity of $v_{\text{exp}} = 150$ km s $^{-1}$. We fit a function of $N_{\text{HI}} = n^* (z^* / \exp(z))^p \exp(-\exp(z)/z^*) / z^*$ to these N_{HI} estimates at $z = 0 - 6$, where p , n^* , and z^* are free parameters. We obtain the best-fit parameters of $n^* = 1.25 \times 10^{21}$ cm $^{-2}$, $p = 0.52$, and $z^* = 329$. In Figure 10, the black solid curve represents the best-fit function, and the gray shaded area exhibits the N_{HI} range of the best-fit function that is allowed in the outflow velocity range of $v_{\text{exp}} = 50 - 200$ km s $^{-1}$. Figure 10 indicates that N_{HI} decreases from $z \sim 0$ to 6, and the best-estimate N_{HI} values at $z \sim 0, 2$, and 6 are $\sim 7 \times 10^{19}$, $\sim 3 \times 10^{19}$, and $\sim 1 \times 10^{18}$ cm $^{-2}$, respectively. Our N_{HI} estimates agree with the one obtained by the independent approach of Pardy et al. (2014), which is presented in Figure 10. Pardy et al. (2014) measure N_{HI} of star-forming galaxies at $z \sim 0.1$ with the H I imaging and spectroscopic data of the 100m Green Bank Telescope. Hashimoto et al. (2015) also estimate N_{HI} with Ly α line profiles of galaxies at $z \sim 2$ based on the high resolution spectra, and these N_{HI} estimates are similar to those of our study. The agreements between our results and these studies suggest that our N_{HI} estimates are reasonably reliable. In Figure 10, we find that the N_{HI} decrease with dust extinction of Ly α resonant scattering can explain the large $f_{\text{esc}}^{\text{Ly}\alpha}$ increase at $z \sim 0 - 6$, even if we allow the uncertainty of the outflow velocity measurements. The picture of the N_{HI} decrease is consistent with the increase of the ionization parameter towards high- z suggested by Nakajima & Ouchi (2014). Because high- z galaxies with a high ionization parameter may have density-bounded nebulae (see Figure 12 of Nakajima & Ouchi 2014), a large fraction of neutral hydrogen in ISM is ionized, which shows a small N_{HI} . The N_{HI} decrease is also consistent with the picture that the ionizing photon escape fraction increases towards high- z (e.g., Inoue et al. 2006; Ouchi et al. 2009; Dijkstra et al. 2014; Nakajima & Ouchi 2014). Our results suggest that the large $f_{\text{esc}}^{\text{Ly}\alpha}$ increase is self-consistently explained by the decreasing N_{HI} , which weakens the ISM dust attenuation through the Ly α resonance scattering. If we assume the expanding shell models, the typical N_{HI} decreases from $\sim 7 \times 10^{19}$ ($z \sim 0$) to $\sim 1 \times 10^{18}$ cm $^{-2}$ ($z \sim 6$).

6. SUMMARY

We have conducted the deep and large-area Subaru/Suprime-Cam imaging survey with the narrow-band filter, NB387. We have observed five independent blank fields of SXDS, COSMOS, CDFS, HDFN, and SSA22

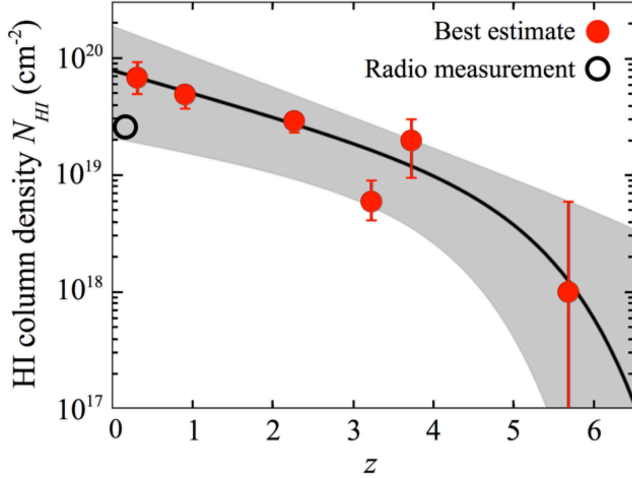


Figure 10. Redshift evolution of the H I column density, N_{HI} , of LAEs, as derived from the 3D Ly α Monte-Carlo radiative transfer code, MCLya. The red filled circles show the best-estimate N_{HI} values for the average outflow velocity of $v_{\text{exp}} = 150 \text{ km s}^{-1}$ (see text). The black solid curve is the best-fit function for these N_{HI} values. The gray shaded area represents the N_{HI} range of the best-fit function allowed for the outflow velocity range of $v_{\text{exp}} = 50 - 200 \text{ km s}^{-1}$. The black open circle denotes the mean N_{HI} value at $z \sim 0.1$ from the radio observations (Pardy et al. 2014).

whose total survey area is $\simeq 1.43 \text{ deg}^2$. We make the sample consisting of 3,137 LAEs at $z = 2.2$, which is the largest LAE sample, to date, that is about an order of magnitude larger than the typical LAE samples in previous studies. The sample covers a very wide Ly α luminosity range of $\log L_{\text{Ly}\alpha} = 41.7 - 44.4 \text{ erg s}^{-1}$ that allows us to determine bright and faint ends of the Ly α LFs. The major findings of our study are summarized below.

1. Using our large LAE sample, we derive the Ly α LFs at $z = 2.2$ with small uncertainties including Poisson statistics and cosmic variance errors (Figure 5). We fit a Schechter function to our best-estimate Ly α LF at $z = 2.2$, and obtain the best-fit Schechter parameters of $L_{\text{Ly}\alpha}^* = 5.29_{-1.13}^{+1.67} \times 10^{42} \text{ erg s}^{-1}$, $\phi_{\text{Ly}\alpha}^* = 6.32_{-2.31}^{+3.08} \times 10^{-4} \text{ Mpc}^{-3}$, and $\alpha = -1.75_{-0.09}^{+0.10}$ with no priori assumptions in the parameters. We find that the faint-end slope of the Ly α LF at $z = 2$ is steep. The faint-end slope is comparable to that of UV-continuum LFs at $z \sim 2$ reported by Reddy & Steidel (2009) and Alavi et al. (2014).
2. In our best-estimate Ly α LF at $z = 2.2$, we find a bright-end hump at $\log L_{\text{Ly}\alpha} \gtrsim 43.4 \text{ erg s}^{-1}$, where the Ly α LF significantly exceeds beyond the best-fit Schechter function (Figure 5). We investigate our LAEs making the bright-end hump with multiwavelength data of X-ray, UV, and radio that are available in the SXDS and COSMOS fields. We find that all of the LAEs at $\log L_{\text{Ly}\alpha} > 43.4 \text{ erg s}^{-1}$ are detected in the X-ray, UV, or radio band. This result indicates that this bright-end hump is not originated from the gravitational lensing magnification bias but AGNs.
3. We identify a moderate but significant increase of the Ly α LF by a factor of $\lesssim 2$ from $z \sim 2$ to 3. We extend our investigation from $z = 2 - 3$ to $z = 0 - 8$ and present the overall evolutionary trends of Ly α LFs: the large increase of the Ly α LFs from $z \sim 0$ to 3, no evolu-

tion of the Ly α LFs at $z \sim 3 - 6$, and the decrease of the Ly α LFs at $z \sim 6$ and beyond. Calculating the Ly α LDs by the integrations of these Ly α LFs, we show that Ly α LDs increase nearly by two orders of magnitude from $z \sim 0$ to 3, and that Ly α LDs decreases by a factor of ~ 2 from $z \sim 6$ to 8 (see also Deharveng et al. 2008; Ouchi et al. 2008; Konno et al. 2014). This increase at $z \sim 0$ to 3 is significantly faster than the one of UV LDs, and the decrease at $z \gtrsim 6$ is more rapid than the one of UV LDs.

4. Based on the LAEs with the detection(s) in the X-ray, UV, or radio band, we derive the AGN UV-continuum LF at $z \sim 2$ down to the faint magnitude limit of $M_{\text{UV}} \sim -22.5$. We find that our AGN UV LF covers a magnitude range fainter than the previous studies with an overlap at $M_{\text{UV}} \simeq -24.8$ with the SDSS DR9 measurements (Ross et al. 2013) and the 2dF-SDSS results (Croom et al. 2009), and confirm that our AGN UV LF agrees well with the SDSS results at the overlap magnitude. Fitting the double-power law function to the AGN UV LF data obtained by our and previous studies, we constrain the faint-end slope of the AGN UV LF at $z \sim 2$, $\alpha_{\text{AGN}} = -1.2 \pm 0.1$, that is flatter than those at $z = 4 - 6.5$, $\alpha_{\text{AGN}} \simeq -1.5 - -1.8$, given by Ikeda et al. (2011); Giallongo et al. (2015).
5. We estimate $f_{\text{esc}}^{\text{Ly}\alpha}$ values from the Ly α and UV LDs at $z \sim 0 - 8$ given by our and previous studies. There is a $f_{\text{esc}}^{\text{Ly}\alpha}$ decrease at $z \gtrsim 6$ that can be explained by the Ly α scattering of the IGM H I at the EoR. We find a large $f_{\text{esc}}^{\text{Ly}\alpha}$ increase from $z \sim 0$ to 6 by two orders of magnitude. This large $f_{\text{esc}}^{\text{Ly}\alpha}$ increase can be explained neither by stellar population nor outflow because there exist no significant evolutions in stellar population and outflow in LAEs at $z \sim 0 - 6$. The dust extinction with no Ly α resonance scattering can partly explain the $f_{\text{esc}}^{\text{Ly}\alpha}$ increase at $z \sim 0 - 6$, but there remains a significantly large discrepancy at $z < 4$. Thus, the Ly α resonance scattering in H I ISM is an important effect to explain the large $f_{\text{esc}}^{\text{Ly}\alpha}$ increase. Based on the average $E(B - V)_{\text{gas}}$ values for non-resonance nebular lines estimated with the observational data, our simple expanding shell models of MCLya suggest that the typical H I column density of ISM should decrease from $\sim 7 \times 10^{19} (z \sim 0)$ to $\sim 1 \times 10^{18} \text{ cm}^{-2} (z \sim 6)$ to explain the large $f_{\text{esc}}^{\text{Ly}\alpha}$ increase.

We thank Hajime Sugai, Daniel Kunth, Nobunari Kashikawa, Tohru Nagao, Shun Saito, and Yuichi Harikane for useful comments and discussions. This work was supported by World Premier International Research Center Initiative (WPI Initiative), MEXT, Japan, and KAKENHI (23244025 and 15H02064) Grant-in-Aid for Scientific Research (A) through Japan Society for the Promotion of Science (JSPS). A.K. acknowledges support from the JSPS through the JSPS Research Fellowship for Young Scientists.

Facility: Subaru (Suprime-Cam)

REFERENCES

- Adams, J. J., Blanc, G. A., Hill, G. J., et al. 2011, *ApJS*, 192, 5
Alavi, A., Siana, B., Richard, J., et al. 2014, *ApJ*, 780, 143

- Alexander, D. M., Bauer, F. E., Brandt, W. N., et al. 2003, *AJ*, 126, 539
- Atek, H., Kunth, D., Schaerer, D., et al. 2014, *A&A*, 561, A89
- Atek, H., Schaerer, D., & Kunth, D. 2009, *A&A*, 502, 791
- Bardeen, J. M., Bond, J. R., Kaiser, N., et al. 1986, *ApJ*, 304, 15
- Barger, A. J., Cowie, L. L., & Wold, I. G. B. 2012, *ApJ*, 749, 106
- Bertin, E. & Arnouts, S. 1996, *A&AS*, 117, 393
- Blanc, G. A., Adams, J. J., Gebhardt, K., et al. 2011, *ApJ*, 736, 31
- Bouwens, R. J., Illingworth, G. D., Oesch, P. A., et al. 2015, *ApJ*, 803, 34
- Brocklehurst, M. 1971, *MNRAS*, 153, 471
- Bruzual, G. & Charlot, S. 2003, *MNRAS*, 344, 1000
- Calzetti, D., Armus, L., Bohlin, R. C., et al. 2000, *ApJ*, 533, 682
- Capak, P., Aussel, H., Ajiki, M., et al. 2007, *ApJS*, 172, 99
- Capak, P., Cowie, L. L., Hu, E. M., et al. 2004, *AJ*, 127, 180
- Cardamone, C. N., van Dokkum, P. G., Urry, C. M., et al. 2010, *ApJS*, 189, 270
- Carroll, S. M., Press, W. H., & Turner, E. L. 1992, *ARA&A*, 30, 499
- Cassata, P., Le Fèvre, O., Garilli, B., et al. 2011, *A&A*, 525, A143
- Cassata, P., Tasca, L. A. M., Le Fèvre, O., et al. 2015, *A&A*, 573, A24
- Ciardullo, R., Gronwall, C., Adams, J. J., et al. 2013, *ApJ*, 769, 83
- Ciardullo, R., Gronwall, C., Wolf, C., et al. 2012, *ApJ*, 744, 110
- Ciardullo, R., Zeimann, G. R., Gronwall, C., et al. 2014, *ApJ*, 796, 64
- Cowie, L. L., Barger, A. J., & Hu, E. M. 2010, *ApJ*, 711, 928
- , 2011, *ApJ*, 738, 136
- Cowie, L. L. & Hu, E. M. 1998, *AJ*, 115, 1319
- Croom, S. M., Richards, G. T., Shanks, T., et al. 2009, *MNRAS*, 399, 1755
- Dawson, S., Rhoads, J. E., Malhotra, S., et al. 2007, *ApJ*, 671, 1227
- Deharveng, J.-M., Small, T., Barlow, T. A., et al. 2008, *ApJ*, 680, 1072
- Dietrich, M., Hamann, F., Shields, J. C., et al. 2002, *ApJ*, 581, 912
- Dijkstra, M., Wyithe, S., Haiman, Z., et al. 2014, *MNRAS*, 440, 3309
- Ellis, R. S., McLure, R. J., Dunlop, J. S., et al. 2013, *ApJ*, 763, L7
- Elvis, M., Civano, F., Vignali, C., et al. 2009, *ApJS*, 184, 158
- Erb, D. K., Steidel, C. C., Trainor, R. F., et al. 2014, *ApJ*, 795, 33
- Finkelstein, S. L., Rhoads, J. E., Malhotra, S., et al. 2009, *ApJ*, 691, 465
- Fiore, F., Puccetti, S., Grazian, A., et al. 2012, *A&A*, 537, A16
- Furusawa, H., Kosugi, G., Akiyama, M., et al. 2008, *ApJS*, 176, 1
- Gawiser, E., van Dokkum, P. G., Gronwall, C., et al. 2006, *ApJ*, 642, L13
- Gehrels, N. 1986, *ApJ*, 303, 336
- Giacconi, R., Rosati, P., Tozzi, P., et al. 2001, *ApJ*, 551, 624
- Giallongo, E., Grazian, A., Fiore, F., et al. 2015, *A&A*, 578, A83
- Gronke, M., Dijkstra, M., Trenti, M., et al. 2015, *MNRAS*, 449, 1284
- Gronwall, C., Ciardullo, R., Hickey, T., et al. 2007, *ApJ*, 667, 79
- Guaita, L., Acquaviva, V., Padilla, N., et al. 2011, *ApJ*, 733, 114
- Guaita, L., Gawiser, E., Padilla, N., et al. 2010, *ApJ*, 714, 255
- Gunn, J. E. & Stryker, L. L. 1983, *ApJS*, 52, 121
- Hashimoto, T., Ouchi, M., Shimasaku, K., et al. 2013, *ApJ*, 765, 70
- Hashimoto, T., Verhamme, A., Ouchi, M., et al. 2015, *ApJ*, 812, 157
- Hathi, N. P., Ryan, Jr., R. E., Cohen, S. H., et al. 2010, *ApJ*, 720, 1708
- Hayashino, T., Matsuda, Y., Tamura, H., et al. 2004, *AJ*, 128, 2073
- Hayes, M., Östlin, G., Duval, F., et al. 2014, *ApJ*, 782, 6
- Hayes, M., Östlin, G., Schaerer, D., et al. 2010, *Nature*, 464, 562
- Hayes, M., Schaerer, D., Östlin, G., et al. 2011, *ApJ*, 730, 8
- Hildebrandt, H., Erben, T., Dietrich, J. P., et al. 2006, *A&A*, 452, 1121
- Hinshaw, G., Larson, D., Komatsu, E., et al. 2013, *ApJS*, 208, 19
- Hopkins, P. F., Hernquist, L., Cox, T. J., et al. 2006, *ApJ*, 639, 700
- Hu, E. M., Cowie, L. L., & McMahon, R. G. 1998, *ApJ*, 502, L99
- Ikeda, H., Nagao, T., Matsuoka, K., et al. 2011, *ApJ*, 728, L25
- Inoue, A. K., Iwata, I., & Deharveng, J.-M. 2006, *MNRAS*, 371, L1
- Iye, M., Ota, K., Kashikawa, N., et al. 2006, *Nature*, 443, 186
- Jones, T., Stark, D. P., & Ellis, R. S. 2012, *ApJ*, 751, 51
- Kashikawa, N., Nagao, T., Toshikawa, J., et al. 2012, *ApJ*, 761, 85
- Kashikawa, N., Shimasaku, K., Malkan, M. A., et al. 2006, *ApJ*, 648, 7
- Kashikawa, N., Shimasaku, K., Matsuda, Y., et al. 2011, *ApJ*, 734, 119
- Kennicutt, Jr., R. C. 1998, *ApJ*, 498, 541
- Kinney, A. L., Calzetti, D., Bohlin, R. C., et al. 1996, *ApJ*, 467, 38
- Konno, A., Ouchi, M., Ono, Y., et al. 2014, *ApJ*, 797, 16
- Kornei, K. A., Shapley, A. E., Erb, D. K., et al. 2010, *ApJ*, 711, 693
- Kusakabe, H., Shimasaku, K., Nakajima, K., et al. 2015, *ApJ*, 800, L29
- Lai, K., Huang, J.-S., Fazio, G., et al. 2008, *ApJ*, 674, 70
- Madau, P. 1995, *ApJ*, 441, 18
- Madau, P., Pozzetti, L., & Dickinson, M. 1998, *ApJ*, 498, 106
- Malhotra, S. & Rhoads, J. E. 2002, *ApJ*, 565, L71
- Mason, C. A., Treu, T., Schmidt, K. B., et al. 2015, *ApJ*, 805, 79
- Matsuda, Y., Yamada, T., Hayashino, T., et al. 2004, *AJ*, 128, 569
- Matthee, J., Sobral, D., Santos, S., et al. 2015, *MNRAS*, 451, 400
- McCracken, H. J., Capak, P., Salvato, M., et al. 2010, *ApJ*, 708, 202
- Meurer, G. R., Heckman, T. M., & Calzetti, D. 1999, *ApJ*, 521, 64
- Miller, N. A., Bonzini, M., Fomalont, E. B., et al. 2013, *ApJS*, 205, 13
- Miyazaki, S., Komiyama, Y., Sekiguchi, M., et al. 2002, *PASJ*, 54, 833
- Mo, H. J. & White, S. D. M. 2002, *MNRAS*, 336, 112
- Murayama, T., Taniguchi, Y., Scoville, N. Z., et al. 2007, *ApJS*, 172, 523
- Nakajima, K. & Ouchi, M. 2014, *MNRAS*, 442, 900
- Nakajima, K., Ouchi, M., Shimasaku, K., et al. 2012, *ApJ*, 745, 12
- , 2013, *ApJ*, 769, 3
- Nilsson, K. K., Tapken, C., Møller, P., et al. 2009, *A&A*, 498, 13
- Nonino, M., Dickinson, M., Rosati, P., et al. 2009, *ApJS*, 183, 244
- Oesch, P. A., Bouwens, R. J., Carollo, C. M., et al. 2010, *ApJ*, 725, L150
- Oke, J. B. 1974, *ApJS*, 27, 21
- , 1990, *AJ*, 99, 1621
- Ono, Y., Ouchi, M., Mobasher, B., et al. 2012, *ApJ*, 744, 83
- Ono, Y., Ouchi, M., Shimasaku, K., et al. 2010a, *ApJ*, 724, 1524
- , 2010b, *MNRAS*, 402, 1580
- Ouchi, M., Mobasher, B., Shimasaku, K., et al. 2009, *ApJ*, 706, 1136
- Ouchi, M., Shimasaku, K., Akiyama, M., et al. 2008, *ApJS*, 176, 301
- Ouchi, M., Shimasaku, K., Furusawa, H., et al. 2010, *ApJ*, 723, 869
- Ouchi, M., Shimasaku, K., Okamura, S., et al. 2004, *ApJ*, 611, 660
- Pardy, S. A., Cannon, J. M., Östlin, G., et al. 2014, *ApJ*, 794, 101
- Parsa, S., Dunlop, J. S., McLure, R. J., et al. 2015, *ArXiv e-prints*, arXiv:1507.05629
- Pentericci, L., Fontana, A., Vanzella, E., et al. 2011, *ApJ*, 743, 132
- Pentericci, L., Grazian, A., Fontana, A., et al. 2007, *A&A*, 471, 433
- Pirzkal, N., Malhotra, S., Rhoads, J. E., et al. 2007, *ApJ*, 667, 49
- Planck Collaboration et al. 2015, *ArXiv e-prints*, arXiv:1502.01589
- Polletta, M., Tajer, M., Maraschi, L., et al. 2007, *ApJ*, 663, 81
- Rauch, M., Haehnelt, M., Bunker, A., et al. 2008, *ApJ*, 681, 856
- Reddy, N. A. & Steidel, C. C. 2009, *ApJ*, 692, 778
- Rhoads, J. E., Malhotra, S., Dey, A., et al. 2000, *ApJ*, 545, L85
- Rivera-Thorsen, T. E., Hayes, M., Östlin, G., et al. 2015, *ApJ*, 805, 14
- Ross, N. P., McGreer, I. D., White, M., et al. 2013, *ApJ*, 773, 14
- Santos, M. R., Ellis, R. S., Kneib, J.-P., et al. 2004, *ApJ*, 606, 683
- Sawicki, M. 2012, *MNRAS*, 421, 2187
- Schaerer, D., Hayes, M., Verhamme, A., et al. 2011, *A&A*, 531, A12
- Schechter, P. 1976, *ApJ*, 203, 297
- Schenker, M. A., Ellis, R. S., Konidaris, N. P., et al. 2014, *ApJ*, 795, 20
- Schiminovich, D., Ilbert, O., Arnouts, S., et al. 2005, *ApJ*, 619, L47
- Schinnerer, E., Smolčić, V., Carilli, C. L., et al. 2007, *ApJS*, 172, 46
- Schlegel, D. J., Finkbeiner, D. P., & Davis, M. 1998, *ApJ*, 500, 525
- Scoville, N., Aussel, H., Brusa, M., et al. 2007, *ApJS*, 172, 1
- Shapley, A. E., Steidel, C. C., Pettini, M., et al. 2003, *ApJ*, 588, 65
- Shibuya, T., Kashikawa, N., Ota, K., et al. 2012, *ApJ*, 752, 114
- Shibuya, T., Ouchi, M., Nakajima, K., et al. 2014, *ApJ*, 788, 74
- Shimasaku, K., Kashikawa, N., Doi, M., et al. 2006, *PASJ*, 58, 313
- Simpson, C., Martínez-Sansigre, A., Rawlings, S., et al. 2006, *MNRAS*, 372, 741
- Sobral, D., Matthee, J., Darvish, B., et al. 2015, *ApJ*, 808, 139
- Stark, D. P., Richard, J., Charlot, S., et al. 2015, *MNRAS*, 450, 1846
- Steidel, C. C., Adelberger, K. L., Shapley, A. E., et al. 2000, *ApJ*, 532, 170
- Taniguchi, Y., Ajiki, M., Nagao, T., et al. 2005, *PASJ*, 57, 165
- Treu, T., Schmidt, K. B., Trenti, M., et al. 2013, *ApJ*, 775, L29
- Ueda, Y., Watson, M. G., Stewart, I. M., et al. 2008, *ApJS*, 179, 124
- van Dokkum, P. G. 2001, *PASP*, 113, 1420
- Verhamme, A., Schaerer, D., Atek, H., et al. 2008, *A&A*, 491, 89
- Verhamme, A., Schaerer, D., & Maselli, A. 2006, *A&A*, 460, 397
- Wofford, A., Leitherer, C., & Salzer, J. 2013, *ApJ*, 765, 118
- Wold, I. G. B., Barger, A. J., & Cowie, L. L. 2014, *ApJ*, 783, 119
- Wyithe, J. S. B., Yan, H., Windhorst, R. A., et al. 2011, *Nature*, 469, 181
- Xue, Y. Q., Luo, B., Brandt, W. N., et al. 2011, *ApJS*, 195, 10
- Yagi, M., Kashikawa, N., Sekiguchi, M., et al. 2002, *AJ*, 123, 66
- Yamada, T., Nakamura, Y., Matsuda, Y., et al. 2012, *AJ*, 143, 79
- Zamojski, M. A., Schiminovich, D., Rich, R. M., et al. 2007, *ApJS*, 172, 468
- Zheng, Z.-Y., Finkelstein, S. L., Finkelstein, K., et al. 2013, *MNRAS*, 431, 3589